

# Analysis of the initiation of an extreme North Pacific jet retraction using piecewise tendency diagnosis

Melissa Breeden  | Jonathan E. Martin

Department of Atmospheric and Oceanic Sciences,  
University of Wisconsin-Madison, Madison,  
Wisconsin, USA

## Correspondence

Jonathan E. Martin, Department of Atmospheric  
and Oceanic Sciences University of  
Wisconsin-Madison, 1225 W. Dayton St. Madison,  
WI 53706, USA  
Email: jemarti1@wisc.edu

## Funding information

National Science Foundation, 1265182.

An unusually prolonged retraction of the tropopause-level jet transformed the circulation in the North Pacific for weeks in mid-February and March 2006 and preceded the development of a long-lived negative Pacific–North American pattern. The initiation of this jet retraction, associated with a series of anticyclonic/LC1 wave-breaking events at high latitude, is investigated through the lens of quasi-geostrophic (QG) piecewise tendency analysis. Two key anticyclonic anomalies divert and retract the jet through serial LC1 wave-breaking events, mostly confined to the 315–330 K isentropic layer and occurring in regions of strong deformation. The rapid development of the first anomaly coinciding with the beginning of retraction is diagnosed in a QG framework, in order to quantify contributions to QG height tendencies from various processes. The resultant analysis reveals that growth was induced by a deep potential vorticity intrusion that perturbed the jet, while the remainder of the ridge’s life cycle was largely governed by upper-level deformation in the jet exit region. Deformation facilitated both growth and decay, as the phasing between the ridge and deformation changed. Baroclinic development also contributed to growth but, unlike prior published analyses of anticyclones in the North Pacific, was not the dominant term.

## KEYWORDS

blocking, geophysical fluid dynamics, jet stream variability, midlatitude weather systems

## 1 | INTRODUCTION

The tropopause-level jet stream in the North Pacific is one of the most dynamically influential features on the planet, affecting both the day-to-day sensible weather as well as elements of the low-frequency general circulation around the globe (Namias and Clapp, 1949; Palmén and Newton, 1969). The jet stream varies in strength and position throughout the year, becoming stronger in winter when the Northern Hemisphere meridional temperature gradient intensifies (Palmén, 1948; Fleming *et al.*, 1987; Weickmann and Chervin, 1988; Newman and Sardeshmukh, 1998). In addition to a pronounced seasonal cycle, substantial intraseasonal variability prevails, often associated with high-impact weather including atmospheric blocking and changes in the track and frequency of extratropical cyclones (Rex, 1950; Palmén and Newton, 1969; Dole and Gordon, 1983).

Motivated by the changes in the position and strength of the jet on monthly, weekly and daily time-scales, many studies have investigated coherent modes of variability in the middle-to-upper troposphere that impact the jet. Wallace and Gutzler (1981) investigated the covariance of monthly-mean 500 hPa geopotential height anomalies for December–February 1962–1977, by correlating various base points around the Northern Hemisphere with the two-dimensional height field. Their analysis revealed the presence of large-scale “teleconnection” patterns in which certain geopotential height anomalies separated by great distances varied together, often as dipoles or quadrupoles. In the Pacific basin, the Pacific–North American (PNA) pattern, a quadrupole structure, whose positive phase is characterized by an anticyclonic anomaly in the subtropical central Pacific, a sprawling cyclonic feature to its north in the midlatitudes, followed by another trough–ridge pair downstream over the

west coast of North America and the southeastern United States, prevailed.

Another curious characteristic of the jet is that it can both modulate, and be modulated by, the life cycle of baroclinic eddies. Simmons and Hoskins (1980) used a baroclinic channel model and varied the shear in the domain to investigate how this alteration to the background state affects the life cycle of a prescribed, small-amplitude perturbation. Thorncroft *et al.* (1993) performed a similar experiment at higher resolution, and found that enhancing the cyclonic shear in the domain leads to what they termed an “LC2” type life cycle, wherein a developing cyclone remains on the cyclonic shear side of the jet and continues to rotate cyclonically as it decays. In contrast, the same initial disturbance growing in a basic state characterized by relatively reduced cyclonic shear was observed to migrate from the cyclonic to anticyclonic shear side of the jet, while changing tilt from northwest/southeast (NW/SE) (negative tilt) to NE/SW (positive tilt). In the latter example, a streamer of high, cyclonic potential vorticity (PV) air is cut off while the disturbance decays, reflective of Rossby wave breaking, defined as the reversal of the climatological meridional PV gradient which points south–north in the Northern Hemisphere (McIntyre and Palmer, 1983). Thorncroft *et al.* (1993) dubbed this particular life cycle “LC1”, terminology that has been adopted by many authors since.

Teleconnections, jet variability and wave breaking are physically related, and clarifying the finer points of their relationships is an active area of research. Martius *et al.* (2007) showed how the frequency of LC1/LC2 wave-breaking events, identified via PV streamers on various isentropic surfaces, differed significantly during various phases of well-known teleconnection patterns like the PNA and North Atlantic Oscillation (NAO). Pertinent to the present study is the reduction in LC2 (cyclonic) wave breaking associated with the negative polarity of the PNA, during which time a sprawling anticyclone is present in the central North Pacific and the jet is retracted. Martius *et al.* (2007) found the primary change in wave-breaking frequency on 310 K during the negative PNA occurs in the vicinity of the midlatitude anticyclone, which suppresses baroclinic wave activity and cyclone development in that region. Subtropical (or Kona) cyclogenesis, known to enhance Hawaiian precipitation (Otkin and Martin, 2004), is more frequent during this PNA phase due to the diverted waveguide. Franzke *et al.* (2011) examined the synoptic evolution of each phase of the PNA and found that the negative phase coincides with a weaker jet and a series of anticyclonic wave-breaking events, consistent with the results of Martius *et al.* (2007).

The central Pacific anomalies associated with the PNA are similar to the dipole in the leading mode of upper-level (250–300 hPa) zonal wind speed in the North Pacific region, previously identified using empirical orthogonal function (EOF) analysis (Eichelberger and Hartmann, 2007; Athanasiadis *et al.*, 2010). This mode of variability represents

the zonal extending or retracting of the jet exit region (EOF1), while the second mode indicates a north/south shifting of the exit region (EOF2) (Athanasiadis *et al.*, 2010; Jaffe *et al.*, 2011; Griffin and Martin, 2017). Otkin and Martin (2004) found that the frequency of subtropical cyclones in the basin is greatly modulated by the zonal extent of the upper-level jet, captured by EOF1. In particular, a retracted jet is associated with more-frequent subtropical “Kona Low” systems, consistent with the results of Martius *et al.* (2007). The results from Otkin and Martin (2004) prompted an interest in the evolution of jet retractions in particular, given their association with Hawaiian precipitation.

Jaffe *et al.* (2011; hereafter JM) first defined criteria for a jet retraction using two independent methods, and examined the composite evolution of the three-dimensional flow field before, during and after retraction onset. Retractions were objectively identified when the mean wind speed in a latitude–longitude box in the central Pacific was less than 10 m/s below climatology for at least five consecutive days (box location: 25–40°N, 180–200°E; JM figure 2). This location coincides with the greatest amplitude in the pattern of EOF1 of 300 hPa zonal wind (JM figure 4). Each case was then visually inspected to verify that the objective identification scheme was truly selecting a retraction, and not a north/south shift in a continuous jet core as represented by EOF2. A total of 19 cases were confirmed by both methods from November to March, 1980–2007.

The composite evolution of the tropopause-level PV was detailed by JM and is summarized here (Figure 1). Ten days before retraction onset no distinct upper-level features were observed, while the jet extends past Hawaii (Figure 1a). Five days prior, the jet remains strong and is now accompanied by a cyclone in the left exit region and a high-amplitude ridge located downstream over western North America (Figure 1b). A zonally elongated, anticyclonic PV anomaly is observed on the poleward side of the jet entrance region over northern China. At retraction onset, an equivalent barotropic, sprawling anticyclone in the midlatitude central Pacific develops and extends from the tropopause level to the surface (Figure 1c). The anticyclone is accompanied by a zonally elongated cyclonic anomaly to its south in the subtropics, and together the circulation of these two features is ideally located to create anomalous easterly winds that counter the westerly jet and coincide with a retracted state. Five days following retraction, a cyclonic anomaly centred over British Columbia and anticyclonic feature over the southern United States have developed, while the central Pacific anomalies are stronger than at retraction onset (Figure 1d). Ten days following retraction onset, the anomalies observed 5 days prior are still observed but weaker in magnitude (Figure 1e). Overall the anomaly pattern at Day +5 and Day +10 resembles that associated with the negative PNA pattern. However, how the anomaly pattern reverses over the 5 days leading up to retraction was unclear from composite analysis, even looking at the daily evolution. Therefore, the present case-study seeks

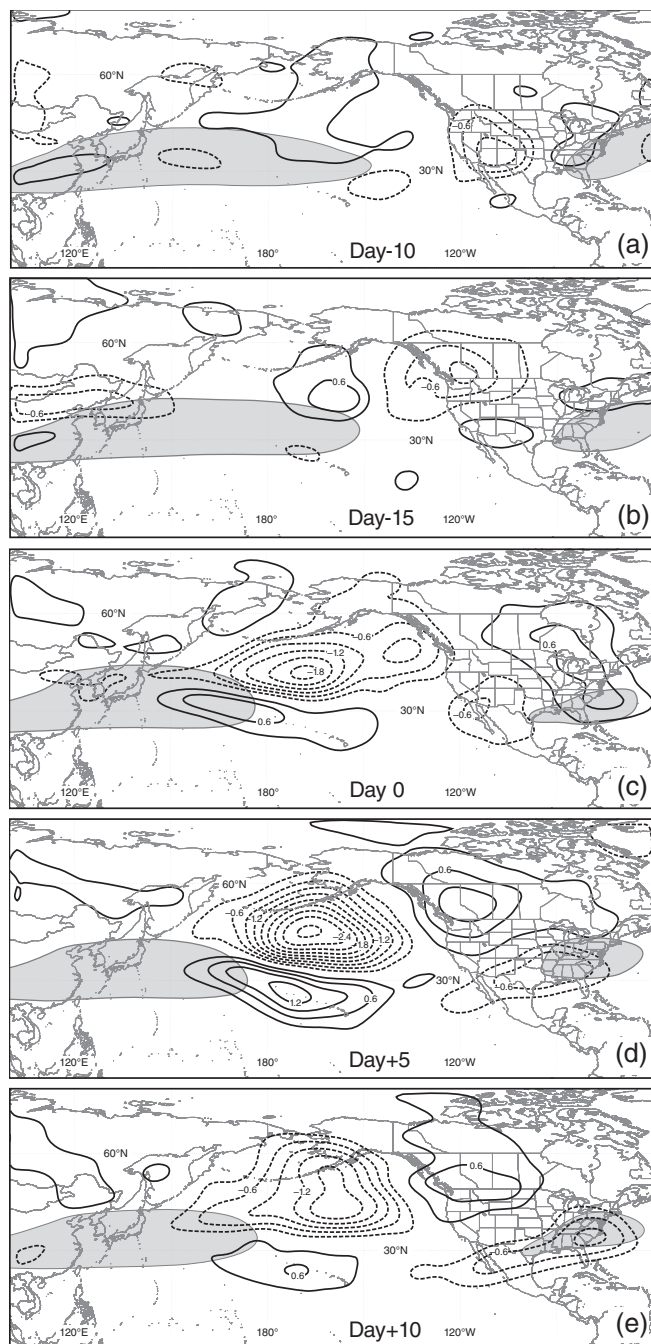


**FIGURE 1** Composite 200–250 hPa Ertel potential vorticity anomalies associated with a jet retraction event at days (a) –10, (b) –5, (c) 0, (d) +5, (e) +10. Solid (dashed) lines indicate positive (negative) PV, contoured every 0.3 PVU ( $1 \text{ PVU} = 10^{-6} \text{ m}^2 \text{ K kg}^{-1} \text{ s}^{-1}$ ) with the zero line removed. Grey shading represents the  $40 \text{ m s}^{-1}$  isotach of the composite 250 hPa zonal wind. Adopted from Jaffe *et al.* (2011)

to reveal additional information regarding the dynamics that *initiate* the transition of the jet to a retracted state.

This study examines the initiation of a jet retraction that occurred from February to March 2006, and led to an unprecedented period of rainfall, flooding and mudslides in Hawaii (Jayawardena *et al.*, 2012). This retraction was extreme in terms of its persistence and overall reduction in the zonal wind speed, ranking first and third, respectively, in those categories (JM). Of particular interest are the links

between jet variability, wave breaking, and the PNA. This article will provide a synoptic overview of the 2006 case and investigate the life cycle of a high-amplitude ridge that facilitated retraction. A second article will use the same case to examine the role of features identified in the synoptic overview, and how they contributed to jet retraction. In this article, section 2 will outline the data and methodology employed in the analysis, and section 3 will provide a synoptic overview of the case. Piecewise tendency diagnosis, first introduced by Nielsen-Gammon and Lefèvre (1996), will then be applied to understand the life cycle of a key feature related to retraction in section 4. Discussion and conclusions will follow in section 5.

## 2 | DATA AND METHODOLOGY

### 2.1 | Data

The ensuing analysis employs European Centre for Medium-range Weather Forecasting (ECMWF) ERA-Interim gridded data that was accessed via the online archive (Dee *et al.*, 2011). Geopotential was accessed on pressure levels from 1,000 to 50 hPa at intervals of 50 hPa and at  $1^\circ \times 1^\circ$  spatial resolution and six-hourly temporal resolution. The dynamic tropopause was considered in terms of Ertel potential vorticity on the 2 PVU surface (1 PVU (unit) =  $10^{-6} \text{ K kg}^{-1} \text{ m}^2 \text{ s}^{-1}$ ). Potential temperature ( $\theta$ ) on 2 PVU is output by ECMWF, found by searching below 98 hPa for the 2 PVU value, and then evaluating  $\theta$  at that location (Berrisford *et al.*, 2011). The first empirical orthogonal function (EOF) of daily mean 250 hPa zonal wind was computed using ERA-Interim data at  $1.5^\circ \times 1.5^\circ$  spatial resolution for November–March, 1979–2014. The EOFs were computed after the 35-year daily climatology was removed. The daily-mean Pacific–North American pattern index was accessed from the Climate Prediction Center (CPC) online archive and was calculated using Rotated Principal Component Analysis introduced by Barnston and Livezey (1987). Both the first principal component time series and PNA index were standardised and then smoothed with a five-day boxcar smoother.

### 2.2 | Anomaly calculations

Standardised height anomalies were computed using ERA-Interim output, by calculating the 1979–2016 average for each six-hour time step. This climatology was then subtracted from the total height field, and the resulting anomalies were standardised with respect to the standard deviation at each grid point. Potential temperature anomalies on the 2 PVU surface were calculated in the same manner, and then the four six-hourly anomalies for each day were averaged to produce a daily anomaly. The potential temperature anomalies were not standardised.

### 2.3 | Piecewise tendency diagnosis

The quasi-geostrophic (QG) system can be used to arrive at a useful relationship between quasi-geostrophic potential vorticity (QGPV) and geopotential (Charney and Stern, 1962). QGPV is the sum of the planetary vorticity, geostrophic relative vorticity, and a stability term,

$$q = f + \frac{1}{f_0} \nabla^2 \phi + f_0 \frac{\partial}{\partial p} \left( \frac{1}{\sigma} \frac{\partial \phi}{\partial p} \right) = f + \mathcal{L}(\phi). \quad (1)$$

The sum reduces to the three-dimensional Laplacian of geopotential ( $\mathcal{L}(\phi)$ ) and planetary vorticity (Equation 1). Here,  $\nabla^2 = \left( \frac{\partial^2}{\partial x^2} + \frac{\partial^2}{\partial y^2} \right)$ , the two-dimensional Laplacian,  $\phi$  represents deviations from the reference atmosphere geopotential,  $f$  is the Coriolis parameter, and  $\sigma$  is the reference atmosphere static stability ( $\sigma = -\frac{\alpha}{\theta} \frac{d\theta}{dp}$ ), where  $\alpha$  is specific volume.

Holopainen and Kaurola (1991) and Hakim *et al.* (1996) demonstrated the utility of partitioning the total QGPV field into a basic state and perturbations around that basic state, and then inverting the perturbation QGPV,  $q'_{\text{tot}}$ , to retrieve the balanced geopotential height field, from

$$\phi'_{\text{tot}} = \mathcal{L}^{-1}(q'_{\text{tot}}). \quad (2a)$$

As  $\mathcal{L}$  is a linear operator,  $q'_{\text{tot}}$  can be split into components that linearly combine to the sum, without any loss of information. Here  $q'_{\text{tot}}$  is split into two pieces, one from an upper layer extending from 50 to 500 hPa, ( $q'_u$ ), and one from a lower layer stretching from 550 to 1,000 hPa, ( $q'_l$ ),

$$\phi'_{\text{tot}} = \phi'_u + \phi'_l = \mathcal{L}^{-1}(q'_u) + \mathcal{L}^{-1}(q'_l). \quad (2b)$$

The circulation associated with each piece of the perturbation QGPV extends throughout the troposphere and is distinguishable using this technique.

Additionally, surface potential temperature at the lower boundary is incorporated after Bretherton (1966), who demonstrated that a positive (negative)  $\theta$  anomaly at the surface can be represented as a positive (negative) QGPV anomaly. Here surface  $\theta$  effects are incorporated through a Neumann boundary condition (Equation (3)) as in Nielsen-Gammon and Lefèvre (1996)<sup>1</sup>:

$$\frac{\partial \phi}{\partial p} = -\frac{R}{p} \left( \frac{p}{p_0} \right)^{\kappa} \theta. \quad (3)$$

Hakim *et al.* (1996) introduced a prognostic piecewise QGPV inversion wherein geostrophic QGPV advection is

<sup>1</sup>One further modification is made to retain the consistency between each  $q'$  field (upper/lower) and the surface  $\theta$  field used in the inversion. Previous studies balance the surface  $\theta$  field with only  $q'_l$  but there is also a piece of surface  $\theta$  that is associated with  $q'_u$  (a smaller but nonnegligible contribution). In the present case the two surface  $\theta$  fields are separated, and each QGPV piece is inverted with its corresponding  $\theta$  field at the lower boundary. The surface  $\theta$  fields are distinguished by first inverting  $q'_l$  with a Dirichlet lower boundary condition, in which the observed geopotential height anomaly is prescribed in the solution. The difference in surface  $\theta$  calculated using the resultant height field and (3a), and that attained by inverting the *unpartitioned*  $q'_{\text{tot}}$  field is attributed to  $q'_u$ , and has a magnitude of +/- 5 K (~25% of the observed 1,000 hPa temperature anomalies).

inverted to attain QG height tendencies. Nielsen-Gammon and Lefèvre (1996, hereafter NGL) further partitioned the advection term to quantify the contributions made by specific processes to the total QG height tendencies. They demonstrated the utility of this method, Piecewise Tendency Diagnosis (PTD), through a rigorous investigation of the development of a mobile trough over the United States.

The mathematical steps taken to arrive at an expression for piecewise QG height tendencies are repeated here. First, the Eulerian time tendency of QGPV reduces to the three-dimensional (3D) Laplacian of height tendencies (Equation (4)), so that inverting the local QGPV tendency field yields QG height tendencies, (Equation (5)):

$$\frac{\partial q}{\partial t} = \frac{1}{f_0} \nabla^2 \left( \frac{\partial \phi}{\partial t} \right) + f_0 \frac{\partial}{\partial p} \left( \frac{1}{\sigma} \frac{\partial}{\partial p} \left( \frac{\partial \phi}{\partial t} \right) \right) = \mathcal{L} \left( \frac{\partial \phi}{\partial t} \right), \quad (4)$$

$$\frac{\partial \phi}{\partial t} = \mathcal{L}^{-1} \left( \frac{\partial q}{\partial t} \right) = \mathcal{L}^{-1}(-\mathbf{v}_g \cdot \nabla q). \quad (5)$$

Assuming adiabatic and frictionless flow, QGPV is conserved following the geostrophic flow, and geostrophic QGPV advection can be substituted for the local time tendency  $\frac{\partial q}{\partial t}$  (right-hand side of Equation (5), where  $\mathbf{v}_g = [u_g \mathbf{i} + v_g \mathbf{j}]$  and represents the geostrophic wind vector). The advection can be further separated into several terms that represent distinct physical processes by partitioning advection into a basic state ( $\bar{\mathbf{v}}_g, \bar{q}$ ) and anomalous ( $q', \mathbf{v}'_g$ ) QGPV and geostrophic wind fields. These fields are then further split into upper ( $q'_u, \mathbf{v}'_{gu}$ ) and lower ( $q'_l, \mathbf{v}'_{gl}$ ) layers as previously described. For this case, only the terms that advect the upper-level QGPV are retained, in order to diagnose upper-level height tendencies, as done in NGL, resulting in

$$\begin{aligned} & i \qquad \qquad \qquad ii \qquad \qquad \qquad iii \\ \frac{\partial \phi'_u}{\partial t} &= \mathcal{L}^{-1}(-\bar{\mathbf{v}}_g \cdot \nabla q'_u) + \mathcal{L}^{-1}(-\mathbf{v}'_{gu} \cdot \nabla \bar{q}_u) + \mathcal{L}^{-1}(-\mathbf{v}'_{gl} \cdot \nabla \bar{q}_u) \\ & iv \qquad \qquad \qquad v \\ & + \mathcal{L}^{-1}(-\mathbf{v}'_{gu} \cdot \nabla q'_u) + \mathcal{L}^{-1}(-\mathbf{v}'_{gl} \cdot \nabla q'_u). \end{aligned} \quad (6)$$

The basic/mean/background state is defined as the five-day time mean from 11 to 15 February 2006, the period just prior to retraction onset. The anomalous geostrophic wind fields associated with the upper and lower layers,  $\mathbf{v}'_{gu}$  and  $\mathbf{v}'_{gl}$ , were calculated using the geopotential fields attained from inverting  $q'_u$  and  $q'_l$ , including their respective surface potential temperature anomalies according to

$$\mathbf{v}'_{gu} = \frac{1}{f_0} \mathbf{k} \times \nabla (\mathcal{L}^{-1}(q'_u)), \quad (7a)$$

$$\mathbf{v}'_{gl} = \frac{1}{f_0} \mathbf{k} \times \nabla (\mathcal{L}^{-1}(q'_l)). \quad (7b)$$

Equation (6) shows the terms that contribute to the upper layer (500–50 hPa) QG height tendencies only; six additional terms of similar form can be determined for the low-level QG height tendency field. Term *i* represents the advection of upper level perturbation QGPV,  $q'_u$ , by the background

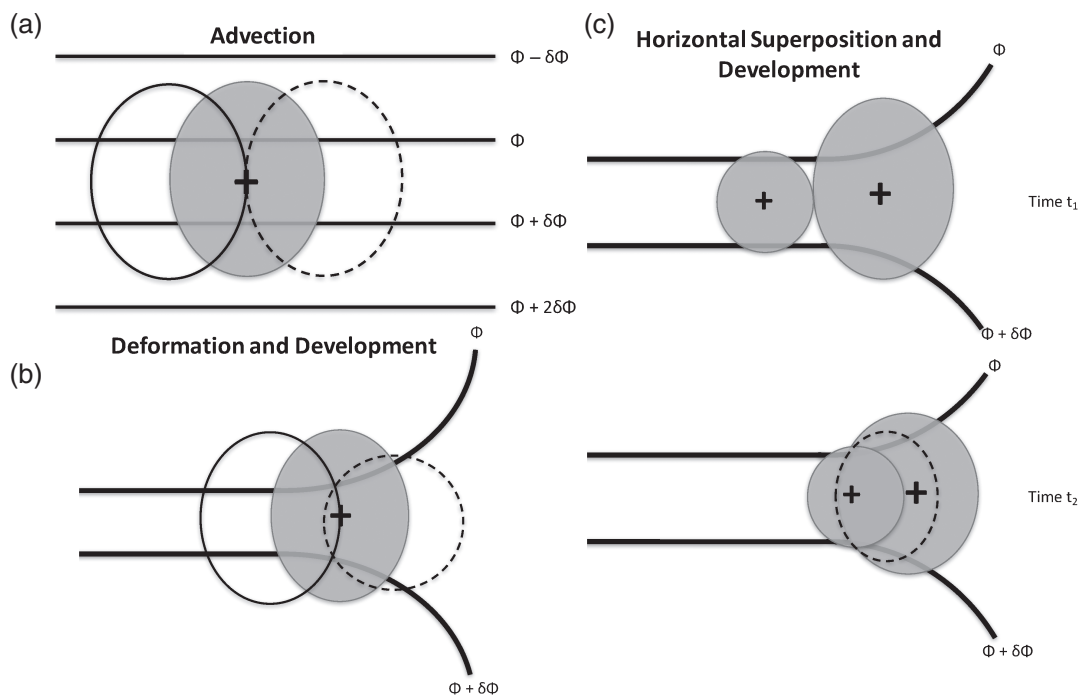


**FIGURE 2** Northern Hemisphere schematics for processes included in Term  $i$  in Equation (6). (a) Advection of a theoretical, positive (cyclonic) QGPV anomaly situated within a symmetric, geostrophic background flow, with the location of positive (negative) height tendencies shown in solid black (dashed black) open circles. (b) Development due to diffuence in the background flow. Note the change in the shape of the height tendencies, indicating development due to the overlap of tendencies and the centre of the QGPV anomaly. (c) Development due to the horizontal superposition of separate anomalies, differentially advected by the geostrophic background flow, resulting in overlap at  $t_2$

geostrophic winds  $\bar{v}_g$ . This term includes effects from the advection, deformation, and superposition of anomalies by the background flow (Figure 2). The mean wind will always tend to advect disturbances downstream, which leads this term to be high in magnitude and also flank the sides of the anomaly (Figure 2a). Development can occur due to asymmetry in the mean state, often manifested as confluence or diffuence (Figure 2b). The shape of a QGPV anomaly situated in an asymmetric background state can be rearranged, changing its attendant circulation. If the feature becomes more isotropic, the circulation will strengthen, and vice versa. The effect from the horizontal and vertical overlapping of QGPV anomalies, which may be brought together by the mean flow to superpose, is also included in Term  $i$  (horizontal example, Figure 2c). Term  $i$  will be referred to as the deformation/superposition term.

Term  $i$  has a barotropic component which can be isolated by setting the winds at all levels equal to their value at a certain level, here 300 hPa (middle of the upper layer), and inverting the resultant advection. Doing so eliminates any advection caused by vertical wind shear that may exist in the background state, effectively prescribing the wind field to be barotropic. Height tendencies that remain after taking the difference between the unpartitioned  $\bar{v}_g$  wind field and this barotropic component are attributed to vertical wind shear. Vertical shear can differentially advect anomalies so that they vertically overlap and strengthen the circulation of a particular feature, inducing growth. NGL consider development associated with this component of Term  $i$  to be a sign of transient,

“non-modal growth”. Transient growth occurs when the tilt of anomalies with height changes over time, leading to the vertical overlapping of anomalies of the same sign (versus “modal” growth which occurs given a fixed tilt with height over time).

Term  $ii$  represents the advection of upper-level background QGPV,  $\bar{q}_u$ , by the circulation associated with upper-level QGPV anomalies,  $v'_{gu}$ . This term can be important at the leading edge of a wave packet, where individual waves have different amplitudes, leading to asymmetric  $\bar{q}_u$  advection, such that the waves at the front of the packet grow due to the effect of higher-amplitude anomalies upstream (Figure 3). NGL found that this term contributed to the early stages of development of an upper-level trough in their case, and interpreted this development as resulting from Rossby wave energy propagating into the area from upstream at the leading edge of a wave packet. By virtue of these allusions to downstream development or group velocity effects, we refer to this term as the downstream development term, following NGL.

Term  $iii$  represents the effect of low-level perturbation QGPV,  $q'_l$ , and its associated tropospheric-deep circulation  $v'_{gl}$ , on  $\bar{q}_u$ . Given favourable phasing (i.e. westward tilt with height) between upper- and lower-layer anomalies, the circulation associated with a low-level feature (such as a surface cyclone) can advect  $\bar{q}_u$  and amplify a disturbance in the upper troposphere. Accordingly, Term  $iii$  is commonly interpreted as including effects from baroclinic development and is referred to as such in this article. Terms  $iv$  and  $v$  represent nonlinear interactions between the upper- and lower-level

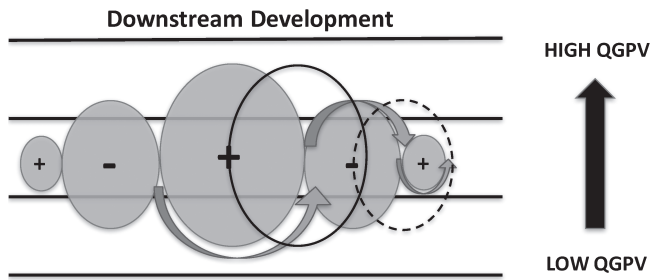


**FIGURE 3** Schematic for Term *ii* in Equation (6), downstream development. The circulation associated with QGPV anomalies in a wave packet situated within a background QGPV gradient will advect the background QGPV, with the influence of the largest anomaly in the centre of the packet leading to the growth of the smaller feature downstream. The largest black solid circle represents the positive height tendencies associated with the largest, centre QGPV anomaly, cyclonic here (for the Northern Hemisphere), which advects low QGPV into the centre of the smaller anticyclonic feature downstream, leading to height rises and development. Similarly, negative height tendencies (dashed black line) would occur downstream of the negative (anticyclonic) QGPV anomaly, due to advection of high background QGPV by the northerly circulation associated with the anticyclonic anomaly

anomalous geostrophic circulations and QGPV anomalies, and depend heavily upon the geometry of the flow field. These two terms involve the anomalous circulation ( $\mathbf{v}'_{gu}$  or  $\mathbf{v}'_{gl}$ ) rearranging  $q'_u$ , and represent height tendencies that arise due to vortex–vortex interactions.

Over-relaxation techniques were employed to solve for the height tendencies associated with each term, which can be linearly combined to quantify the overall piecewise QG tendency. Finally, to confirm that the QG height tendency components are able to account for the “observed” development of  $\phi'_u$ , the height tendency values from the sum of all piecewise terms (Equation 6) were compared against the centred finite-differenced approximation to  $\frac{\partial \phi'_u}{\partial t}$  using the  $\phi'_u$  field (Equation (8)) after all fields were smoothed with a 25-point spatial smoother:

$$QG_{\text{obs}} = \frac{\phi'_u(t+1) - \phi'_u(t-1)}{2dt}. \quad (8)$$

PTD is applied to an important feature associated with the initiation of a rapid jet retraction that began in mid-February 2006. The basic/mean/background state is defined as the five-day time mean from 11 to 15 February 2006, the period just prior to retraction onset. After an overview of the case is presented in section 3, results from PTD are shown in section 4.

### 3 | SYNOPTIC OVERVIEW

The North Pacific jet retraction that began in mid-February 2006 was related to a period of extreme rainfall over Hawaii that continued throughout March (Table 1 JM; Jayawardena *et al.*, 2012). The Federal Emergency Management Agency (FEMA) declared the event a natural disaster due to the resultant flooding, mudslides and damages (FEMA Case

No.1640). The rapid onset of the precipitation broke a dry spell over Hawaii that had been associated with a strong, zonal jet. A synoptic overview of the initiation of this event is given in terms of tropopause maps and Hovmüller diagrams.

#### 3.1 | Tropopause maps

Consideration of potential temperature on the 2 PVU surface, the dynamic tropopause, presents a succinct overview of the upper-tropospheric dynamical evolution (Morgan and Nielsen-Gammon, 1998) and forms the basis of the analysis of the 5 days leading up to retraction (Figures 4 and 5). Figure 4 shows the 1979–2016 February climatology, with three  $\theta$  contours highlighted. The strong west Pacific jet stream is evident where the meridional  $\theta$  gradient is strongest, while its exit region is indicated by the diffluence of the  $\theta$  contours near 160°W. Higher  $\theta$  values are present in the subtropics, signifying a higher, potentially warmer tropopause. Values of  $\theta$  decrease moving poleward, in some places over a short distance, indicating where the tropopause slopes dramatically and wind speeds are highest (as in the west Pacific). A lower, potentially colder tropopause is observed at higher latitude.

Daily mean  $\theta$  anomalies, along with the 315, 330 and 345 K contours, are shown in Figure 5 for 11–19 February. A positive  $\theta$  anomaly on the 2 PVU surface represents an anticyclonic anomaly, while a negative  $\theta$  anomaly signifies anomalous cyclonic flow. Beginning on 11 February, a strong and zonal jet reached 160°W, as implied by the tight and zonally oriented bundle of closely spaced isentropes (Figure 5a). Two high-amplitude ridges characterized by positive  $\theta$  anomalies bookended the jet, one upstream of the jet entrance region labelled B, the other located downstream over northwestern Canada and Alaska. A small, zonally elongated positive  $\theta$  anomaly was situated within the jet over southern Japan, labelled A. The following day Feature B moved southeastward and encountered the jet entrance region, perturbing the zonal jet and inducing waves (Figure 5b). Coinciding with B reaching the jet entrance region, Feature A developed rapidly into a high-amplitude, large-scale, wave-number three ridge by 15 February (Figure 5b–e). This was the first day on which the Jaffe *et al.* (2011) jet retraction criteria were met and occurred when A was at its peak magnitude and amplitude. Feature A’s emergence from the subtropics into the midlatitudes first displaced the jet exit region and initiated the weakening of the zonal wind, by diverting the 315 K contour northward, weakening the  $\theta$  gradient on the dynamic tropopause and thus weakening the tropopause-level geostrophic wind.

From 11 to 15 February, B moved southeastward, its shape changing from nearly circular on 11 February to zonally elongated by 13 February, as the anomaly was deformed first by confluence in the jet entrance and then by the strong winds in the jet core. Feature A became stationary on 15 February and acquired a positive tilt the next day (Figure 5f), signifying the beginning of an anticyclonic/LC1 wave break over the eastern

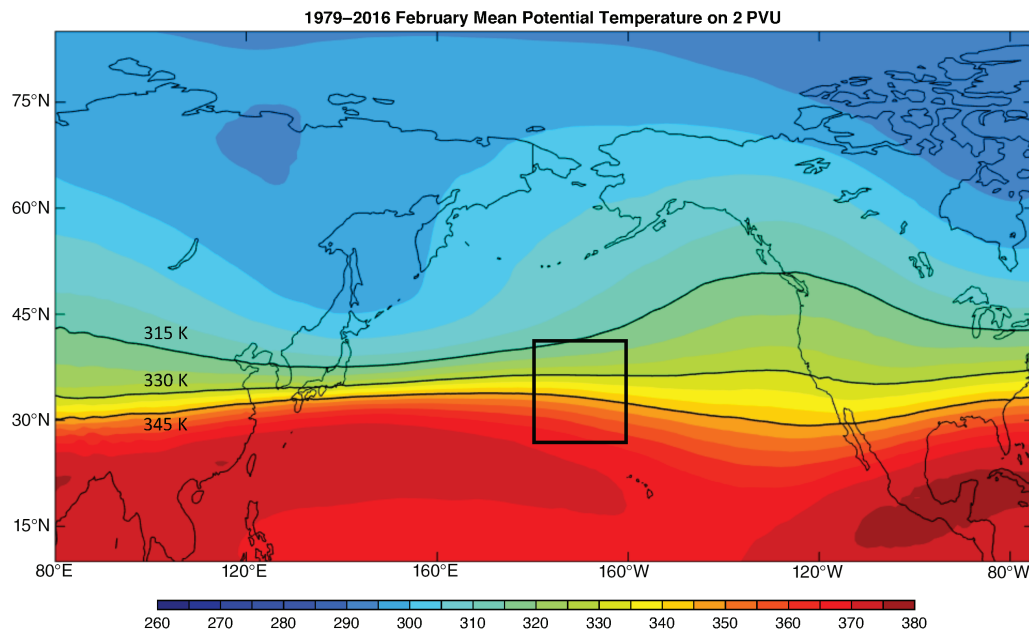


**FIGURE 4** The 38-year (1979–2016) February mean potential temperature on 2 PVU (the dynamic tropopause) from ERA-Interim reanalysis. Fill is potential temperature ( $\theta$ ) in units of K contoured according to the accompanying scale. Solid black contours are the individual 315, 330 and 345 K isentropes. The black square marks the box used by Jaffe *et al.* (2011) to identify retractions

Pacific and western North America.<sup>2</sup> From 14 to 16 February, B hardly moved, remaining situated within the jet and maintaining its oblong shape, while a trough-like feature developed in the subtropics northwest of Hawaii at 330–345 K.

On 17 February, Feature A overturned, as its base remained in the eastern Pacific with its crest farther downstream over the Canadian archipelago. Feature B was located near the date-line and was more isotropic than 1 day earlier (Figure 5g). Over the next 2 days (Figure 5h–i) A and B merged, as B encroached upon the nearly stationary A. The deformation associated with the jet exit region was, by 19 February, located near 160°E, a combined result of the evolution of A and the emergence of B out of the jet core. The subtropical central Pacific remained characterized by a potent, stationary trough on 330–345 K from 15 to 19 February and long thereafter (Figure 5e–i). The trough diverted flow southward in the central Pacific, and, in concert with the ridge to its north, enhanced the deformation associated with the jet exit region, now much farther upstream than on 11 February. The development of the subtropical trough also coincided with the beginning of the rainy period over Hawaii (Jayawardena *et al.*, 2012).

To summarize, 5 days prior to retraction the jet was strong and zonal, and was subsequently split due to anticyclonic anomalies A and B, which both displaced the 315 K contour northward and reduced the meridional tropopause potential temperature gradient on the dynamic tropopause. Both A and B halted in the east-central Pacific in regions of high-amplitude deformation, and were associated with a

period of anticyclonic wave breaking on 315 K at rather high latitude and low altitude (low  $\theta$ ). To the south of these two anticyclonic features, stationary cyclonic anomalies developed in the subtropics, repeatedly inundating Hawaii with heavy precipitation.

### 3.2 | Hovmüller

A succinct overview of the flow transition associated with the jet retraction is evident in Hovmüller diagrams of 300 hPa standardised height anomalies averaged over 20–30°N and 40–50°N (Figure 6). In the subtropics (Figure 6a), the first half of February was characterized by higher than normal heights from about 130 to 180°E, which were then replaced by negative, cyclonic anomalies after 15 February for the remainder of the month and much of March. These low height anomalies were centred near the date-line and coincided with the persistent, heavy precipitation over Hawaii. Also of note is how stationary the anomalies were, reflective of a dipole-type block. The midlatitude region (Figure 6b) in early February was characterized by many progressive systems as evidenced by cyclonic anomalies moving quickly from west to east over a short period of time. The high-amplitude ridge observed on 11 February at 240°E (Figure 5a) developed and remained stationary from 5 to 11 February, when the jet was zonal and reached the eastern Pacific. Thereafter, “A” formed farther upstream at 200°E and similarly ceased to propagate as observed on the tropopause maps. “B” is also evident as it emerged out of the east as a +2 standard deviation anomaly on 11 February and moved eastward thereafter while “A” remained at 200°E.

After 15 February, the beginning of a long-lived block that persisted until about 10 March is observed. The sprawling

<sup>2</sup>Pelly and Hoskins (2003) showed that wave breaking can be identified when the meridional  $\theta$  gradient reverses, as seen in the 315 K contour on the 16th.

## Potential Temperature Anomalies of the Dynamic Tropopause, February 11–19, 2016

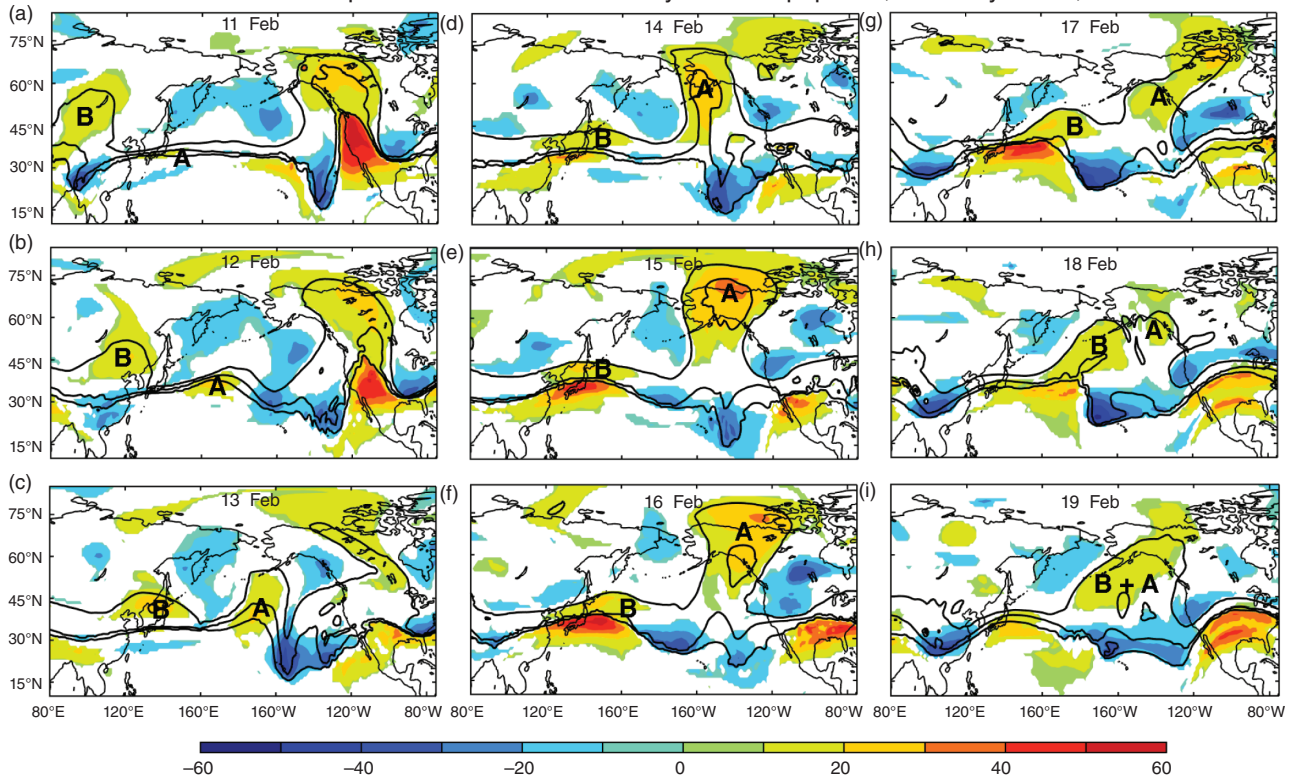


**FIGURE 5** The fill shows daily mean potential temperature anomalies calculated relative to the 1979–2016 daily climatology (fill patterns in units of K contoured according to accompanying scale) on 2 PVU for 11–19 February 2006. Solid black lines show the full-field 315, 330 and 345 K isentropes for (a) 11 February, (b) 12 February, (c) 13 February, (d) 14 February, (e) 15 February, (f) 16 February (g) 17 February, (h) 18 February and (i) 19 February. The “A” and “B” track the positions of two important anticyclonic anomalies discussed in the text. Feature A is the one to which piecewise tendency diagnosis is applied, and the location of the maximum 300 hPa geopotential height anomaly associated with Feature A is shown by the A in (a–e), the period during which the inversion is employed

and potent midlatitude anticyclonic anomaly was contemporaneous with cyclonic anomalies in the subtropics, the two forming a dipole-type block, which maintained the retracted jet. It is of interest that the midlatitude anticyclone was far more expansive zonally (120–200°E) than the subtropical cyclonic feature (170–200°E), indicating that the wavelengths of the two components of the block were rather different. Later in March, the subtropics experienced another period of lower-than-average heights that remained fixed between 180 and 200°E for 15 days. The stationary nature of the anomalies was similar to the earlier period just discussed. Interestingly, the attendant midlatitude behaviour differed from the sprawling, blocked anticyclone that occurred in late February–early March. Rather, a series of progressive ridges interspersed with weak troughs occupied the basin during the latter period, with only one instance of quasi-stationary growth around 15–22 March. Regardless of this difference in the midlatitude complexation compared to earlier in March, the retraction persisted.

### 3.3 | EOF1 and the Pacific–North American pattern

One final perspective is presented to investigate the large-scale flow transition associated with this jet retraction and how it is related to the PNA. Figure 7 shows the 250 hPa zonal wind EOF1 pattern overlaid with the mean jet

position (contours, Figure 7a) and its corresponding PC1 time series, along with the PNA index for February–March 2006 (Figure 7b). The phase of the jet as expressed by this EOF on a given day can be determined by multiplying the value of PC1 on that day by the pattern in Figure 7a. For example, from 10 to 12 February PC1 was slightly positive, indicating that the jet was slightly extended. The PNA index was also positive at this time (note the two time series were calculated using different time periods, so a perfect correspondence between the amplitude of PC1 and the PNA is not anticipated). Thereafter, PC1 rapidly decreased and reached a value of  $-2\sigma$  one week later by 18 February, reflecting the abrupt retraction that occurred. The PNA also rapidly transitioned from positive to negative during this period. Overall there was very good correspondence between retraction onset and the development of the negative PNA phase. Modification of the jet therefore seems important for maintenance and amplification of the PNA pattern, as previous studies have indicated.

## 4 | PIECEWISE TENDENCY DIAGNOSIS

Since the chain of events that led to the prolonged retraction event was initiated by the growth of Feature A, in this section the development of Feature A is diagnosed from the

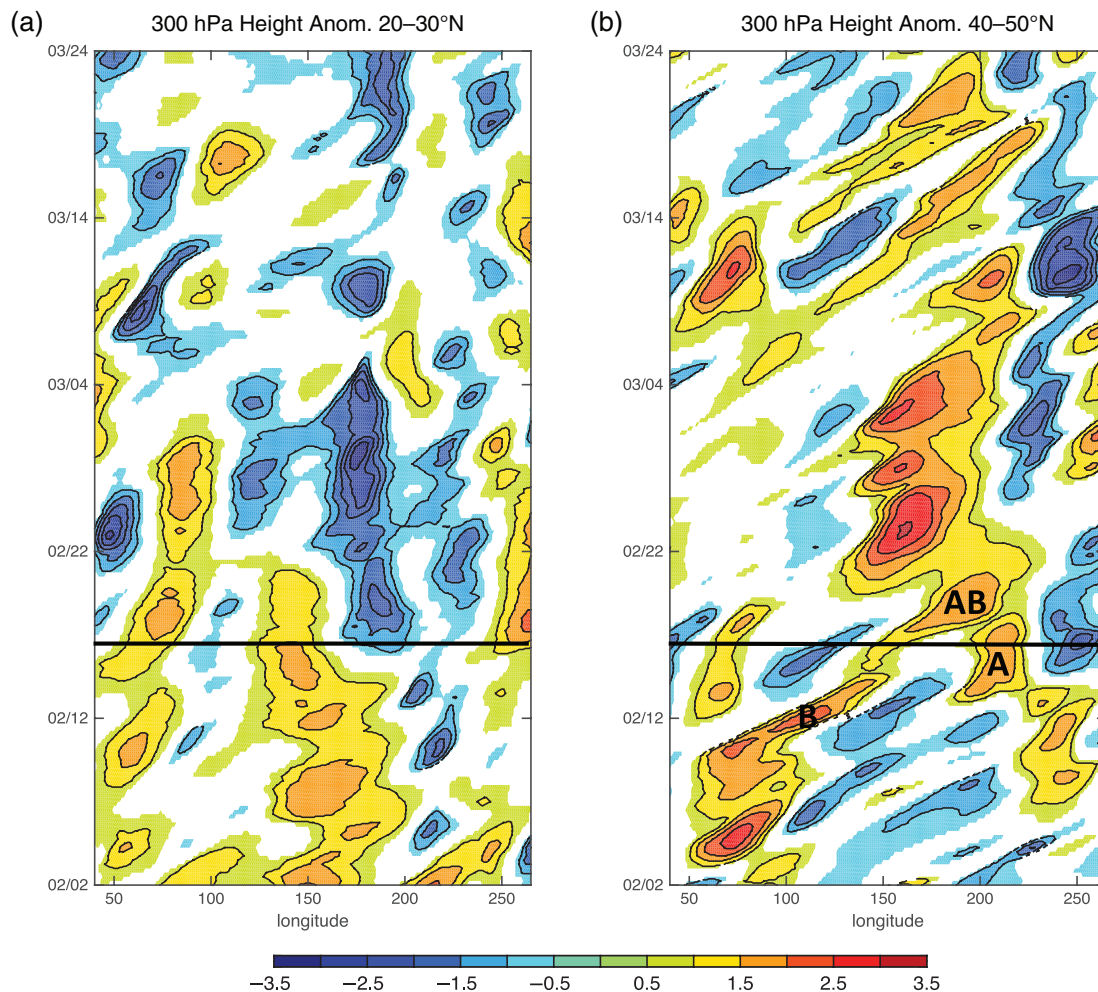


**FIGURE 6** Hovmöller diagrams of standardised 300 hPa height anomalies taken with respect to the 1979–2016 climatology for each day, averaged over (a) 20°–30°N and (b) 40°–50°N for February–March 2006. The black line marks the day that retraction was first identified. Features A and B, discussed in the text, are labelled

QG height tendency perspective using PTD. This section will focus on A's development at 300 hPa, where it was strongest in magnitude.

#### 4.1 | Evaluation of QG diagnosis

The 300 hPa geopotential height anomalies retrieved from inverting the perturbation QGPV, split into two levels using Equation (2b), very closely match those calculated directly using ERA-Interim geopotential, referred to as  $\phi'_a$ . The ERA-Interim geopotential height anomaly was calculated via  $z'_a = \frac{\phi'_a}{g}$ . Figure 8 shows time series tracking the contribution to the maximum height value associated with Feature A using the three height fields<sup>3</sup>  $z'_u$ ,  $z'_l$ , and  $z'_a$ , calculated using  $\phi'_u$ ,  $\phi'_l$ , and  $\phi'_a$ , respectively. The sum of the upper and lower layer contributions adds up to the black dashed line,  $z'_{tot}$ .

<sup>3</sup>At 0600, 1200 UTC 11 February, a distinct height anomaly associated with A has not yet developed as shown in Figure 9b. Instead of tracking the position of maximum  $\phi'_{tot}$ , the grid point of most positive height tendencies, using the  $QG_{obs}$  field, in the region from which Feature A emerges, (marked by the A in Figure 9b) is used. In this way, it is still possible to diagnose the initial development of Feature A.

The extremely close match between the reanalysis anomaly  $z'_a$  (thick black line), and  $z'_{tot}$  (dashed black line) confirms the inversion method was successfully implemented, and shows that both fields undergo substantial development into a 300+ metre ridge during the 5-day period.

From 11–13 February,  $z'_u$  accounts for most of the upper level ridge ( $z'_{tot}$ ), while a substantial contribution on the order of 100 m comes from  $z'_l$  starting at 1200 UTC on the 14th, indicating a low-level ridge had developed and was located directly underneath Feature A at upper levels. To illustrate the evolution of the vertical structure of the circulation near A, Figure 9 shows the 300 hPa and 950 hPa  $z'_{tot}$  fields in black and red, respectively, at 12-hour intervals from 1200 UTC 13 February to 0000 UTC 15 February. At 1200 UTC 13 February, Feature A was amplifying, while a 950 hPa anticyclone had begun to develop to the east of A (labelled H), indicating a characteristic westward tilt with height (Figure 9a). The 300 hPa trough and surface cyclone upstream of A also exhibited westward tilt with height. Over the next 36 h, the 950 hPa ridge amplified to the north but did not propagate eastward, while A amplified and propagated eastward and poleward (Figure 9b–d). By 1200 UTC 14 February, the anticyclones

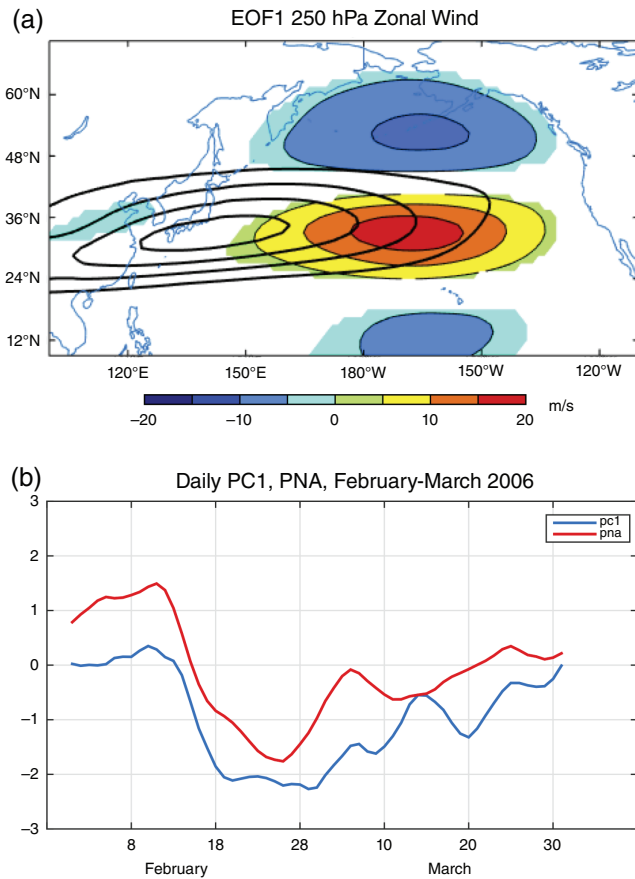


**FIGURE 7** (a) The colour shading shows the EOF1 pattern of 250 hPa zonal wind associated with a 1-sigma deviation in units  $\text{m s}^{-1}$ . The 1979–2014 November–March average 250 hPa zonal isotachs are shown in the solid black lines beginning at  $30 \text{ m s}^{-1}$ , contoured every  $10 \text{ m s}^{-1}$ . (b) Standardised daily mean PC1 associated with EOF1 pattern (blue solid line) and the standardised daily-mean PNA index (red solid line)

were vertically stacked in the eastern Pacific, and remained so at 0000 UTC 15 February. The implications of the change in the vertical structure of feature A from baroclinic to equivalent barotropic will be discussed in section 4.2. However, as the  $z'_u$  field accounted for the majority of the total 300 hPa ridge during its development period from 11 to 13 February, PTD is applied to diagnose the development of the upper-level ridge using Equation (6).

Confirmation that the observed height tendencies, approximated by the finite-difference of the  $\phi'_u$  field (Equation (8)), are reasonably represented by the sum of the QG piecewise terms (Equation (6)) is given in Figure 10. When positive (negative) height tendencies are observed, development (decay) of the ridge is anticipated. The two methods of determining height tendencies, Equations (6) and (8), both indicate that there were positive height tendencies over Feature A until 0000 UTC 14 February, reflecting the rapid development that was observed in the synoptic overview. Overall there is very good agreement between the observed and QG height tendencies, although the QG, piecewise sum sometimes overestimates development or decay. The two time series shown in Figure 10 have a correlation of 0.90, and overall the temporal evolution and general magnitude of amplification match quite

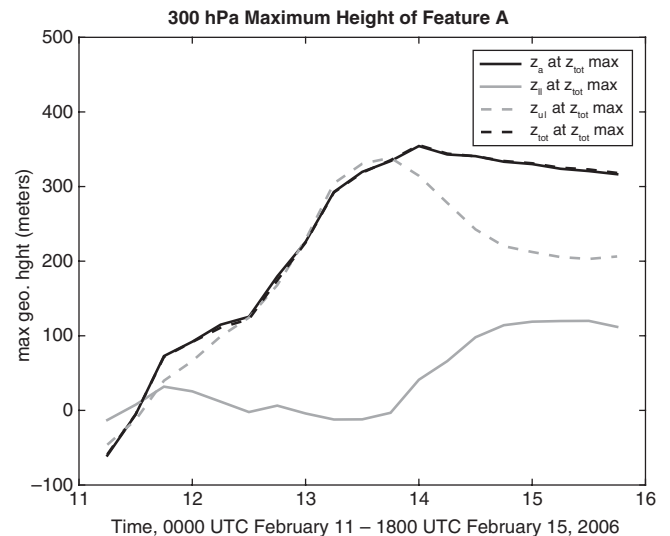


**FIGURE 8** Time series of the maximum 300 hPa geopotential height anomaly associated with feature A using the ERA-Interim reanalysis (solid black line) and various inverted QG height fields (black dash, grey solid, grey dash). Units are metres. The time series are plotted every six hours beginning at 0000 UTC 11 February through to 1800 UTC 15 February 2006. See text for further explanation

well. The processes represented by the QG height tendencies therefore account for the majority of the observed growth of Feature A.

## 4.2 | Components of QG height tendencies

In this section, the terms facilitated development of Feature A through its initial growth period on the 11th, sustained growth thereafter and led to its subsequent weakening are investigated. Negative PV advection into the centre of Feature A drove height rises and amplification and was achieved via several processes during A's life cycle. First, southerly flow on the eastern side of a deep, high-PV intrusion advected low background QGPV northward, and began to produce a positive height anomaly, A, on 11 February. Next, upper-level deformation and superposition, as well as effects from a strong surface cyclone, continued to amplify Feature A through persistent negative PV advection, from 12 to 13 February. Decay of  $\phi'_u$  associated with Feature A occurred on 14 February and was driven by the deformation term, which began to advect *high* PV into the ridge centre and led to height falls over A.

### 4.2.1 | 11 February: Initial growth of Feature A from a PV intrusion

As previously noted, Feature B, a high-amplitude ridge located on the tropopause over Eurasia, reached the poleward side of the jet entrance region on 11 February, and overturned anticyclonically. Figure 11a shows the perturbation QGPV at 1200 UTC 11 February, with B labelled. Downstream of B, a potent, positively tilted 300 hPa trough developed, and a cross-section averaged from 130 to 140°E

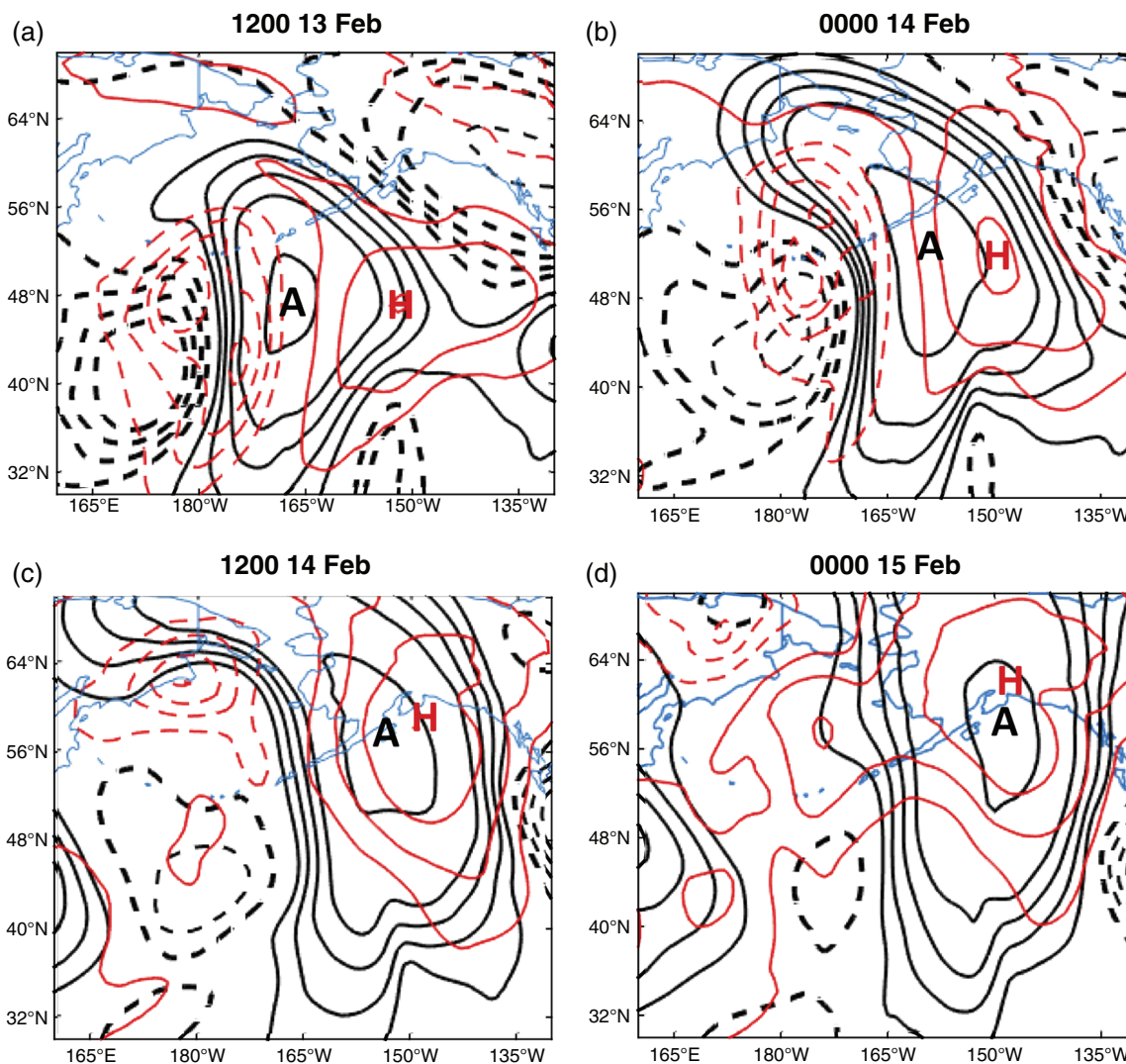


**FIGURE 9** Black (red) contours show 300 hPa (950 hPa)  $z_{\text{tot}}'$  12-hourly from (a) 1200 UTC 13 February to (d) 0000 UTC 15 February 2006. Height anomalies are labelled in m and contoured every 50 m with positive (negative) values in solid (dashed) lines. The “A” denotes the location of Feature A at 300 hPa, and the red H marks the location of the 950 hPa ridge

shows that the trough was linked to a deep intrusion of anomalous high-PV air into the troposphere to 750 hPa (Figure 11b). Overlaid is the background state QGPV, indicating the position of the QGPV intrusion with respect to the strong 300 hPa background QGPV gradient and corresponding jet. While at 300 hPa the cyclonic QGPV anomaly was located north of the jet, the intrusion tilted southward and was located equatorward of the jet at 750 hPa (Figure 11b). Inverting  $q'_l$  between 550–750 hPa isolates specifically the influence of the QGPV intrusion and its associated geopotential height field, which will be referred to as  $z'_{l,\text{intr}}$ . A cross-section of the background state QGPV and meridional wind associated with  $z'_{l,\text{intr}}$ , averaged on the eastern edge of the QGPV intrusion from 140 to 150°E, is shown in Figure 11c. From this cross-section, it is evident that southerly flow on the intrusion’s eastern side reached 300 hPa and was well-positioned to advect low background QGPV northward, inducing positive height tendencies and the development of Feature A.

Figure 12 provides a horizontal view of the QGPV intrusion’s circulation and its position relative to the upper-level

background QGPV at 1200 and 1800 UTC on 11 February, as Feature A is just beginning to develop. The negative height anomaly associated with the QGPV intrusion was centred over southern Japan, and southerly winds on the intrusion’s eastern side crossed the strong background QGPV gradient and transported low background QGPV northward (Figure 12a,b). Inverting the baroclinic development term,  $-\mathbf{v}'_{\text{gl}} \cdot \nabla \bar{q}_u$ , using winds associated *only* with  $z'_{l,\text{intr}}$ , produces positive height tendencies in a broad region to the east of Japan from about 25 to 55°N at both times (Figure 12c,d). The southern extent of the positive height tendencies in the subtropics is the location from which Feature A emerged by 1800 UTC on the 11th (Figure 12d).

The circulation associated with the upper-level trough that was located upstream of A, and was linked to the PV intrusion just discussed, also played a role in A’s initial development (location of trough shown in Figure 12c,d). The downstream development term ( $-\mathbf{v}'_{\text{gu}} \cdot \nabla \bar{q}_u$ ) captures the height tendencies associated with the upper-level trough’s ability to advect the background QGPV. The time series of height tendencies

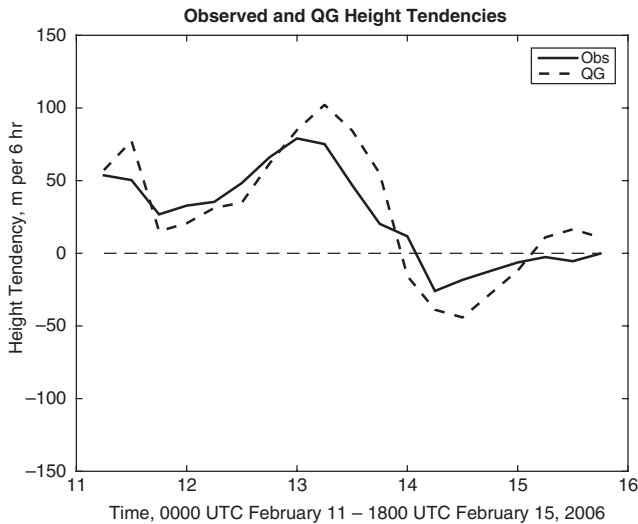


**FIGURE 10** The black solid line shows the time series of the “observed” height tendency of  $\phi'_u$ , calculated using a centred finite difference calculation to produce the  $QG_{\text{obs}}$  height tendency (Equation (8)) evaluated at the position of the maximum value of the total, inverted QG height anomaly (marked in Figure 5a–e by the “A”). The dashed black line shows the sum of piecewise tendencies (Equation (6)) evaluated at the same grid point. The correlation between the two lines is 0.90. Units for height tendencies are  $\text{m} (6\text{h})^{-1}$

associated with advection caused by the upper-level trough and PV intrusion, evaluated at Feature A’s height maximum, are shown in Figure 13. The baroclinic term associated with the intrusion’s circulation (550–750 hPa component of Term *iii* in Equation (6)) and the downstream development term (Term *ii*, Equation (6)), both contributed notably to the growth of A on 11 February. The influence of the PV intrusion weakened but remained positive through 12 and 13 February, while the downstream development term opposed development after 1200 UTC 11 February.

#### 4.2.2 | 12–13 February: Prolonged growth of Feature A via upper-level deformation and superposition, and a surface cyclone

The upper-level trough and PV intrusion also led to the development of a surface cyclone that amplified in the central Pacific from 12 to 14 February (see Figure 9, red dashed contours). The surface cyclone was located upstream of A and downstream of the upper-level trough from 0000 UTC 13 February to 0000 UTC 14 February. The height field attained by inverting  $q'_l$  from 1,000–800 hPa only,  $z'_{l,\text{sfc}}$ , isolates the influence of the surface cyclone, which extended throughout the troposphere. Southerly flow on the cyclone’s eastern side crossed the strong 300 hPa background PV gradient associated with the jet, producing negative  $\bar{q}_u$  advection and height rises. Figure 14 shows the temporal evolution of the height tendency contribution to Feature A’s growth from the 1,000–800 hPa component of the baroclinic development term. Height rises from this term show the cyclone contributed strongly and consistently to the amplification of A until 14 February. After this time, the cyclone propagated northward and away from the strong, 300 hPa background

PV gradient, weakening its ability to influence Feature A (Figure 9c,d).

In addition to the surface cyclone, upper-level deformation strongly contributed to amplification of Feature A from 0000 UTC 12 to 1200 UTC 13 February. The deformation/superposition term,  $-\bar{\mathbf{v}}_g \cdot \nabla q'_u$ , captures the effect of the background circulation advecting and reorganizing upper-level QGPV anomalies, including the negative QGPV anomaly associated with Feature A. High-amplitude deformation is evident in the mean state jet exit region (black contours, Figure 15a), which led the background winds to modify the shape of Feature A, in a manner suggested by the schematic in Figure 2b. Figure 15a shows the  $q'_u$  field at 0000 UTC 13 February along with the background geopotential height contours and associated geostrophic wind. At this time Feature A was situated in between strong, zonal flow on its western side and weak, northward-diverted flow on its eastern side. The position of A in the deformation region is similar to the PV anomaly in the schematic in Figure 2b. It is deduced that the modification of A’s shape by the mean flow increased A’s isotropy at this time, evidenced by height rises due to the deformation/superposition term overlapping with the centre of Feature A (Figure 15b). The height tendency pattern associated with Term *i* resembles a combination of that shown in Figure 2a,b, with height rises mostly downstream of A reflecting advection, but slightly overlapping with A due to the deformation in the mean state. The temporal evolution of the deformation/superposition term shows that deformation amplifies A during its most rapid development period, 12–13 February (Figure 16). Additionally, the *barotropic* component of this term, which captures the effect of horizontal deformation, most strongly amplified Feature A. The barotropic component changed sign and promoted A’s decay starting at 1800 UTC 13 February, discussed in the next subsection.

A positive contribution from the *non-modal* component of the deformation/superposition term to intensifying Feature A is observed in Figure 16 from 0000 UTC 12 February to 1200 UTC 14 February. This indicates that, in addition to horizontal asymmetry in the mean state, vertical shear in the mean state rearranged the three-dimensional  $q'_u$  field in a manner conducive to A’s development. The non-modal component contributed to A’s growth during the period when the vertical tilt between upper- and lower-levels evolved from westward tilted to vertically stacked (Figure 9b–d). The vertical superposition of the negative QGPV anomalies throughout the troposphere, brought together by the vertical shear in  $\bar{\mathbf{v}}_g$ , evidently occurred during this period. Once the upper- and lower-level anticyclones became vertically stacked by 1200 UTC 14 February, this term no longer promoted development of Feature A (Figure 9c,d).

#### 4.2.3 | 14 February: Decay of feature A

As Feature A propagated further into the region of deformation in the eastern Pacific, the direct effect of barotropic

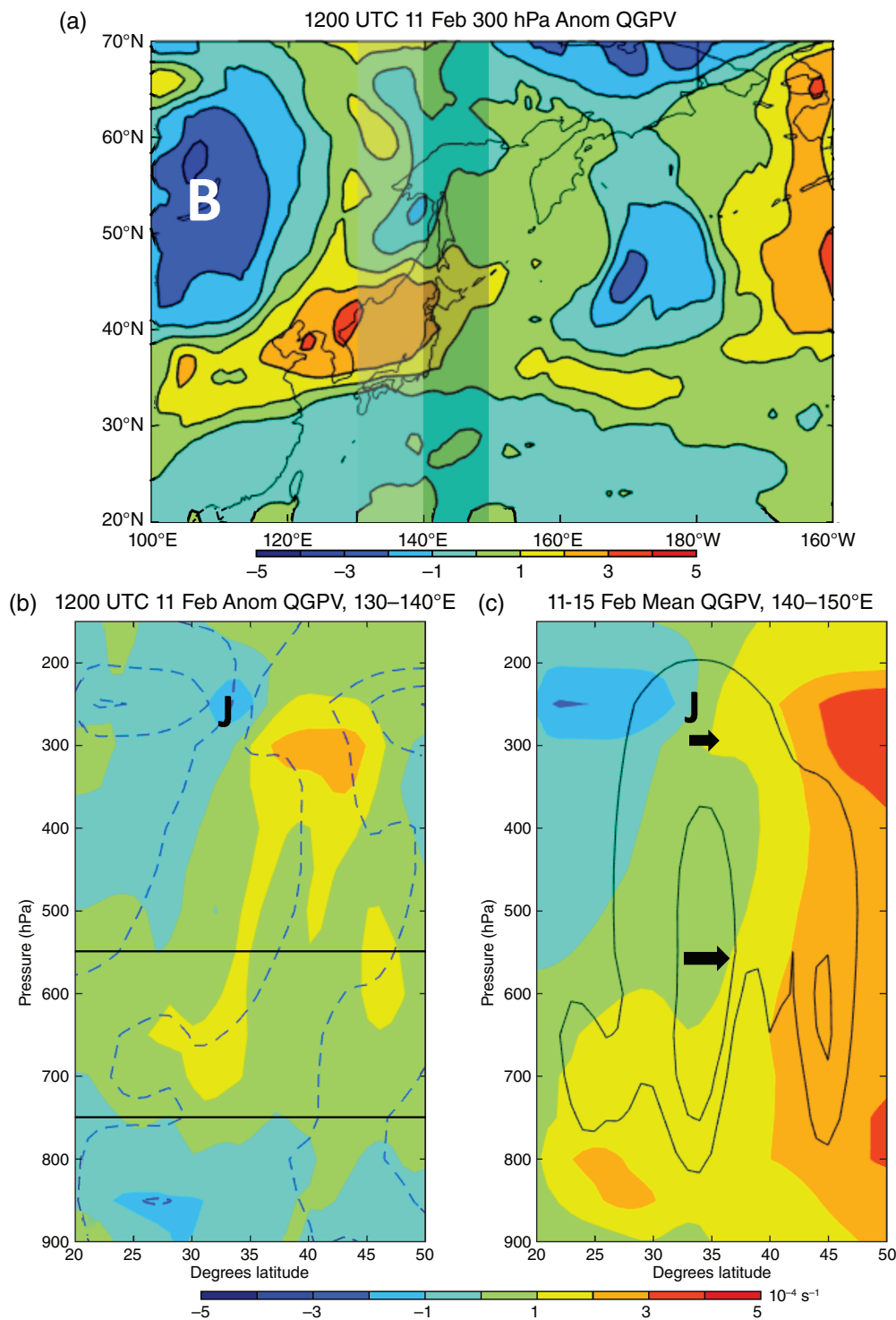


**FIGURE 11** (a) Perturbation QGPV at 1200 UTC 11 February 2006 with location of the averaged cross-section of anomalous QGPV shown in (b) indicated by the light grey box. The dark grey box indicates the location of the cross-section in panel (c). Units for QGPV are  $10^{-4} \text{ s}^{-1}$ . Feature B is labelled. (b) The colour shading shows the meridional cross-section of anomalous QGPV, averaged over 130–140°E at 1200 UTC 11 February. The blue dashed contours indicate the background QGPV, contoured every  $1 \times 10^{-4} \text{ s}^{-1}$ . The black horizontal lines indicate the layer inverted to capture the influence of the intrusion. (c) The colour shading shows the cross-section of the background QGPV, now averaged over 140–150°E, and the black contours show the geostrophic meridional wind associated with the intrusion and  $\phi'_{\text{intr}}$ , contoured at 2 and  $3 \text{ m s}^{-1}$  and indicating southerly flow. The black arrows emphasize the anomalous southerly flow on the eastern edge of the QGPV intrusion shown in the black contours. The location of the jet (J), and associated strong background QGPV gradient, is indicated

deformation transitioned from strengthening to weakening A, as observed in the time series in Figure 16. Feature A, and the trough upstream of A, propagated eastward with time, and positive  $q'_u$  advection associated with the upstream trough strengthened and encroached on Feature A (Figure 17a). As

a result, there were height falls on A's upstream side, which overlapped with the centre of Feature A, inducing height falls and weakening A on the 14th (Figure 17b). Simultaneously, the background geostrophic wind reorganized A's shape such that it became *less* isotropic and its circulation

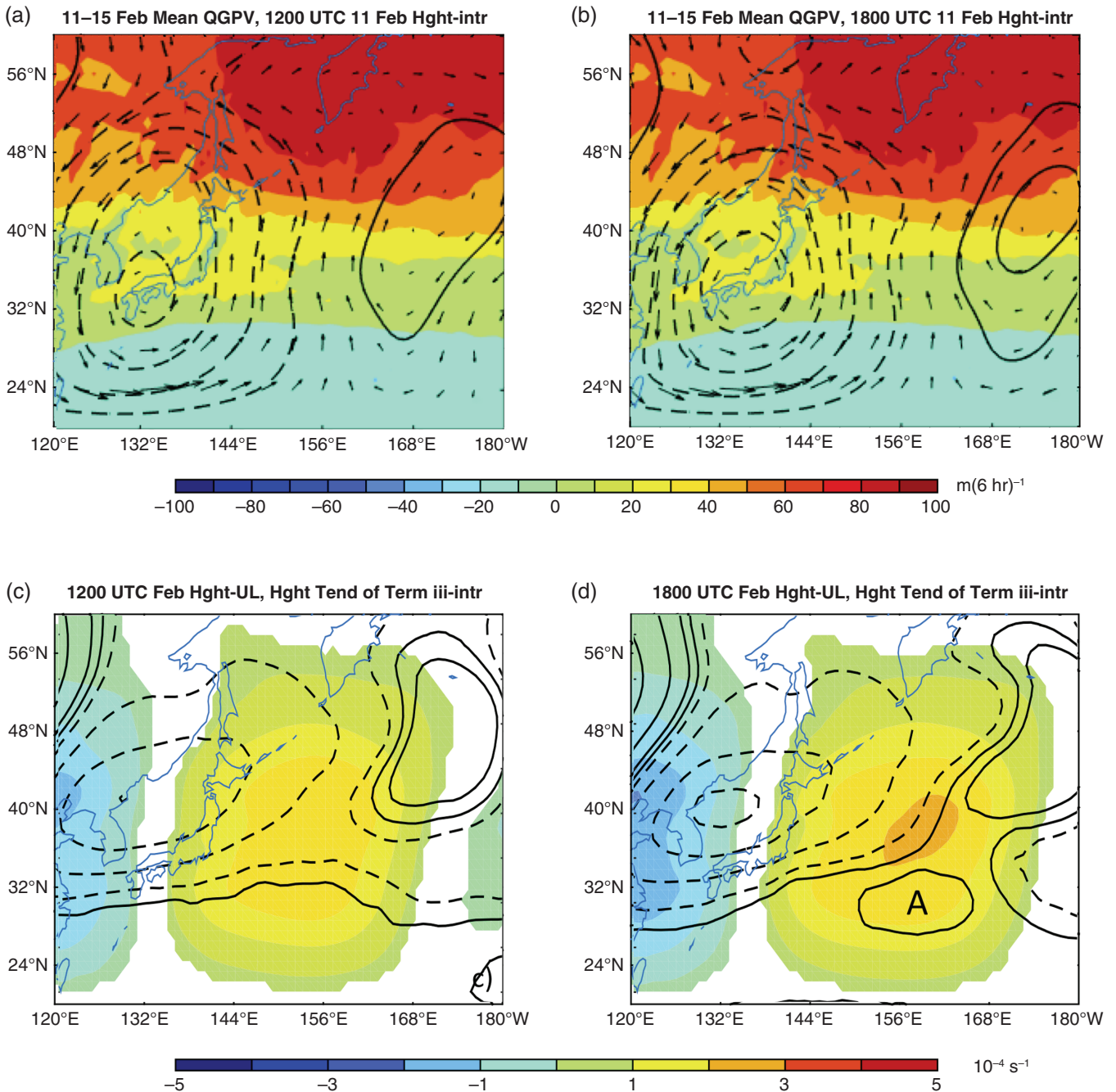


**FIGURE 12** (a) Colour shading is the 11–15 February 2006 mean QGPV field at 300 hPa labelled in units of  $10^{-4} \text{ s}^{-1}$ . Contours are the geopotential height anomalies at 1200 UTC 11 February associated with 550–750 hPa  $q'$  in metres, and contoured at 0,  $\pm 30, 100, 200, 300$ . Solid (dashed) lines indicate positive (negative) height anomalies, and zero is solid. The arrows indicate the flow associated with the anomalous geostrophic circulation calculated using  $\varphi_{\text{intr}}'$ . The corresponding negative background QGPV advection and resulting height rises are shown in (c). (b) As in (a) but for 1800 UTC 11 February. (c) The colour shading is the height tendency pattern resulting from background QGPV advection by the height field shown in (a). The contours are the 300 hPa geopotential height anomalies associated with  $q_u'$ , contoured as in (a). (d) Same as (c) but at 1800 UTC 11 February, with Feature A labelled

was attenuated due to the diffluent flow on A's downstream side.

#### 4.2.4 | PTD summary

The cumulative effect of all processes that contributed to the QG height tendencies associated with Feature A is summarized in Figure 18, which shows time series of all components in Equation (6). First, an upper-level trough and its deep QGPV intrusion initiated development and created a distinct positive height anomaly through negative  $\bar{q}_u$  advection on

its eastern edge (black dashed line). Thereafter, effects from tropopause-level deformation, vertical shear, and a strong surface cyclone caused continued and intense amplification by importing low-PV into Feature A (black dotted and solid grey lines, respectively). A small contribution to growth from the vortex–vortex interaction terms was also observed from 12 to 13 February. Overall, a life cycle emerges wherein downstream development associated with the leading edge of a wave packet, including a tilted, deep PV intrusion, initiated growth and created a positive height anomaly in the subtropics

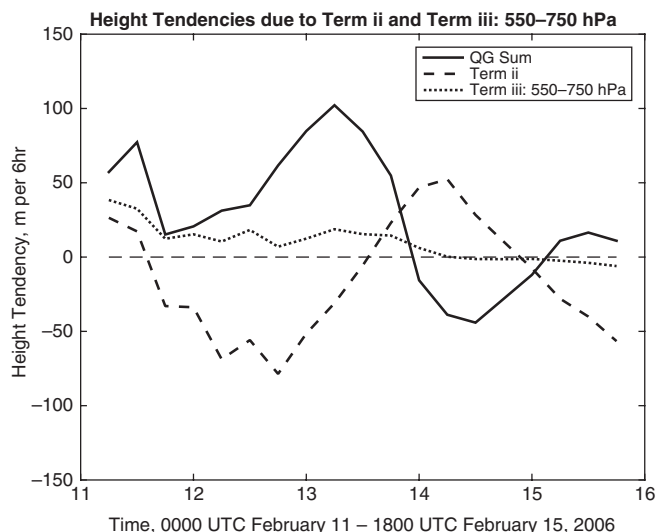


**FIGURE 13** Time series of the height tendencies from downstream development (Term *ii*) and PV intrusion (Term *iii*, 550–750 hPa) at the position evaluated in Figures 7 and 9. Term *ii* in Equation (6) (black dashed line), Term *iii* 550–750 hPa (black dotted line) and the sum of all terms in Equation (6) (solid black line). Units are  $\text{m} (6\text{ h})^{-1}$

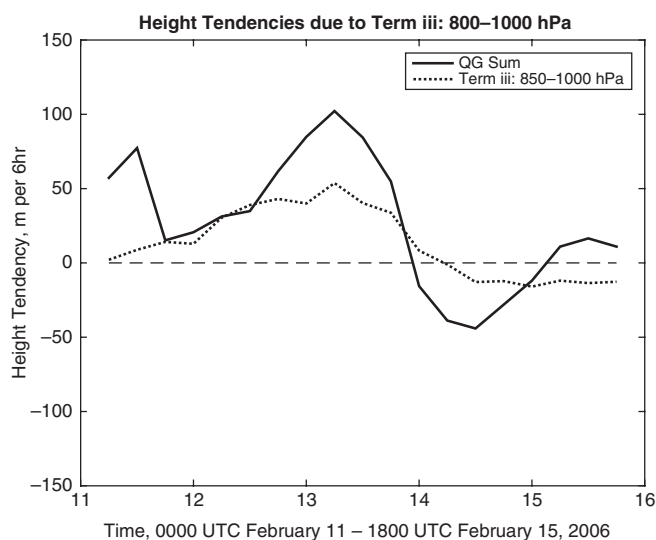


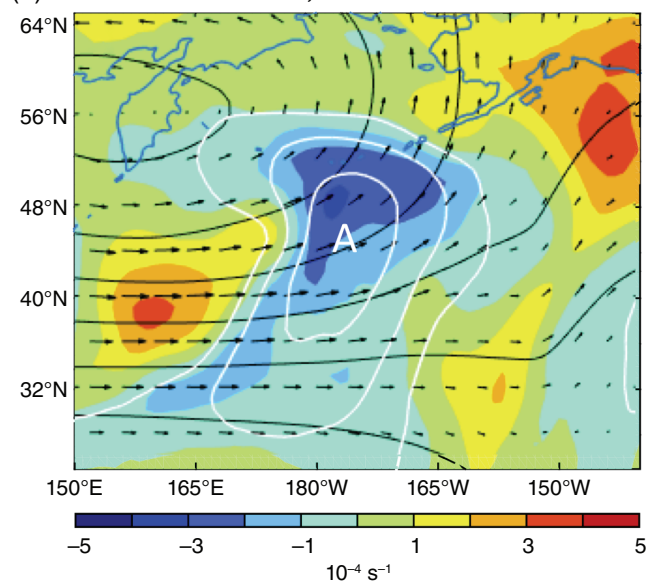
**FIGURE 14** As in Figure 13 except showing the 1,000–800 hPa component of Term *iii* (baroclinic development) shown by the black dotted line

on the equatorward side of the jet. Thereafter, effects from a deformed tropopause and a strong surface cyclone drove development, including a contribution from non-modal growth. Feature A propagated northeastward along  $\overline{\nabla q_u}$  as it amplified, splitting the jet as it propagated, evident in Figure 5c,d. Decay of the upper-level height anomaly associated with A was driven by deformation as well, which began to attenuate the  $q'_u$  anomaly associated with Feature A rather than consolidate it, leading to a weaker anticyclonic anomaly.

## 5 | DISCUSSION AND CONCLUSIONS

This study investigated the initiation of an extreme jet retraction in the North Pacific that transformed the circulation in this basin from one characterized by a progressive storm

**(a) 11–15 Feb Man QGPV, 000 UTC 13 Feb Anom QGPV**



**(b) 0000 UTC 13 Feb Anom Hght, Hght Tend-Term i**

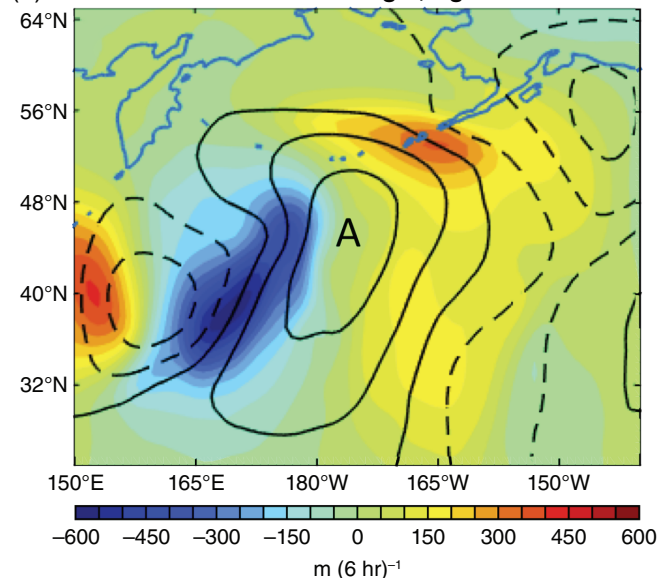


**FIGURE 15** Barotropic deformation. (a) The colour shading shows the 300 hPa  $q'_u$  field on 0000 UTC 13 February 2006, which is being advected by  $\overline{\mathbf{v}}_g$  shown by the black arrows. The white contours show the height anomaly A, and the contour interval is 50 m starting at  $\pm 100$  m, positive values only. (b) The colour shading shows the 0000 UTC 13 February height tendency field from inverting Term *i* in Equation (6),  $(-\overline{\mathbf{v}}_g \cdot \nabla q'_u)$ . Contour interval is 50 m starting at  $\pm 100$  m, positive (negative) is solid (dashed) lines, and zero is solid. The A indicates the location of maximum height of Feature A, and positive tendencies overlapping with A indicates that this term is aiding in further development of A

track and a strong zonal jet, to split, blocked flow in mid-February and March 2006. Retraction onset coincided with the development of a long-lived negative PNA pattern. The initiation of this jet retraction was associated with the development of two key anomalies, A and B, that diverted and retracted the jet through serial LC1 wave-breaking events, mostly confined between 315 and 330 K and occurring in regions of strong deformation. The life cycle of the first wave to break anticyclonically was diagnosed within a QG

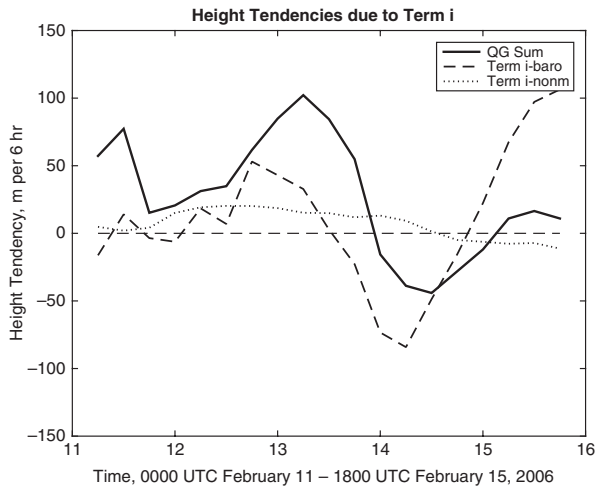


**FIGURE 16** Time series of barotropic (black dashed line) and non-modal (black dotted line) contributions to Term  $i$  in Equation (6). The sum of the right-hand side of Equation (6) is shown in the thick solid black line. Units  $\text{m (6h)}^{-1}$

piecewise tendency framework, and confirmed the physical connections between jet variability, Rossby wave breaking, and the PNA teleconnection pattern revealed in prior studies.

NGL found that downstream development contributed to the amplification of an upper-level mobile trough very early on in the trough's life cycle, when a Rossby wave packet, and its associated energy, propagated into the region from the west. Baroclinic development drove the majority of trough intensification thereafter, while effects from deformation were variable and minimal. Evans and Black (2003) used PTD to diagnose persistent ( $>7$  day duration) 500 hPa anticyclonic anomalies in the North Pacific, the closest analogue to Feature A that has been diagnosed with PTD. During the most rapid development period of the anticyclones they identified, 90% of intensification was associated with baroclinic growth, the other 10% with deformation. Downstream development drove decay of anticyclones in that study, similar to results in NGL, and at no point did this term aid in growth of persistent 500 hPa anticyclones.

In the case presented here, deformation exerted a dominant influence on the growth *and* decay of Ridge A, a result that has not been observed in the Pacific region previously. Additionally, downstream development opposed the effect of deformation, promoting growth when the ridge decayed, in direct opposition to the results of both NGL and Evans and Black (2003) (Figure 18, black dashed line vs. black dotted line). The non-modal contribution to development was persistent but overall about a third of the strength of the barotropic deformation and baroclinic development. Given ongoing discussion regarding the relative roles of instability (evidenced by baroclinic/barotropic growth) versus transient, non-modal growth, we emphasize the utility of PTD to quantify the impact of each process. The fact that all three processes, baroclinic, barotropic and non-modal growth, promoted development and the rapid growth of an upper-level anticyclone that

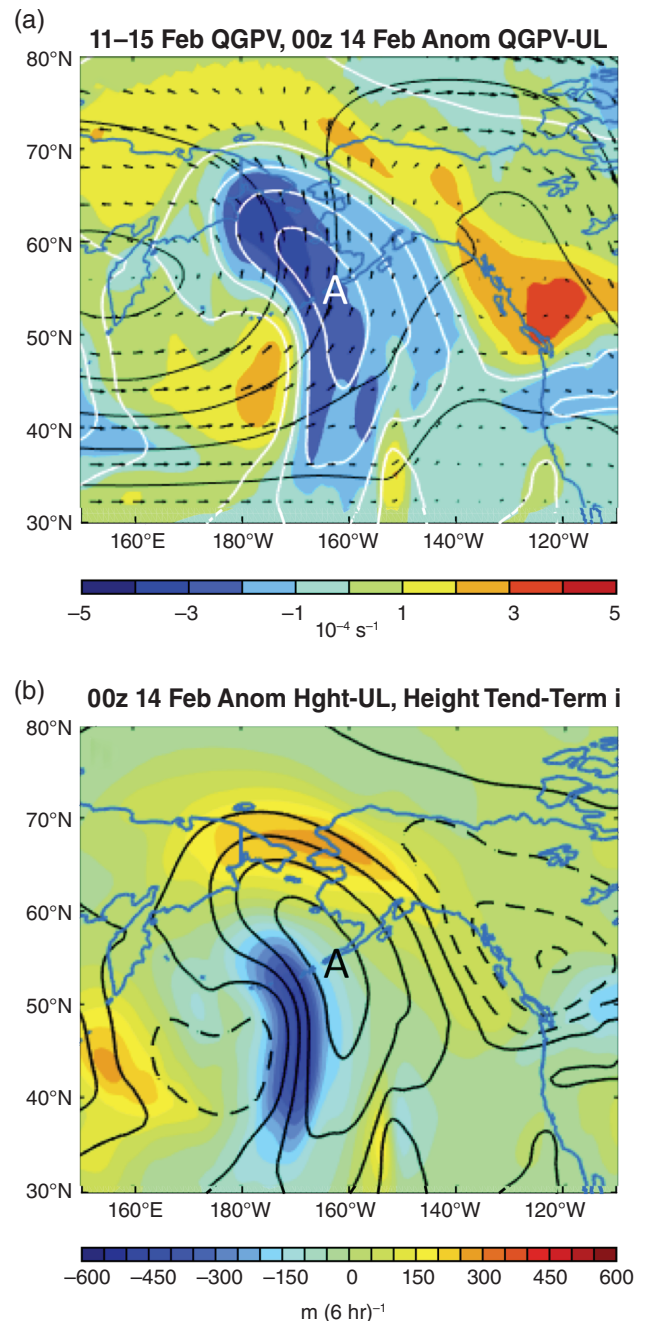


**FIGURE 17** As in Figure 15, but at 0000 UTC 14 February

experiences an LC1 life cycle, has not been investigated in previous studies using PTD.

The mean-state deformation was collocated with a weak meridional QGPV gradient (parallel to the geopotential height gradient in Figure 17a), which is proportional to the zonal phase speed ( $c_x$ ) of a two-dimensional Rossby wave, Equation (9), where  $k$  and  $l$  are the zonal and meridional wave numbers, respectively:

$$c_x - \bar{u} = -\frac{\frac{\partial \bar{q}}{\partial y}}{(k^2 + l^2)}. \quad (9)$$

As Feature A propagated into the region of weak  $\nabla \bar{q}_u$ ,  $\bar{u}$  and its zonal phase speed decreased rapidly. A zonal gradient in the background QGPV was observed on the

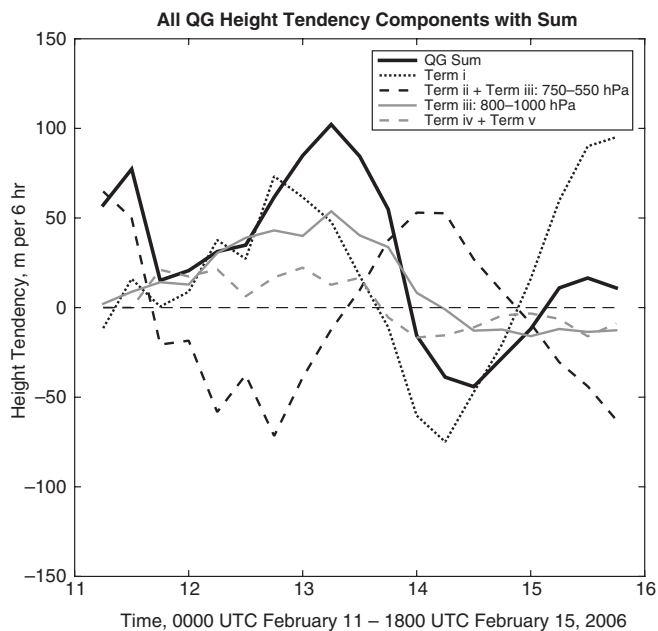


**FIGURE 18** Time series of all terms on the right-hand side of Equation (6). Term *i*, deformation/superposition, is shown by the black dotted line, the sum of Term *ii* (downstream development) and PV intrusion component of Term *iii* (baroclinic development, 750–550 hPa) is by the black dashed line, surface component Term *iii* (baroclinic development, 800–1,000 hPa) is shown by the grey solid line, and the sum of Terms *iv* and *v* (vortex–vortex interactions) is shown by the grey dashed line. The thick black solid line is the sum of all terms in Equation (6)

western edge of the background state deformation, and as a result, A propagated and amplified to the north substantially before becoming stationary and overturning. The downstream development term captures the effect of Rossby wave energy propagation, which is also proportional to the horizontal gradient of  $\bar{q}_u$ . As a result the group velocity was reduced as A reached the weak  $\nabla \bar{q}_u$  in the midlatitude east Pacific. In this case, the change in sign of the downstream development term between 13 and 14 February, coincident with A reaching the region of strong deformation/weak  $\nabla \bar{q}_u$ , is a sign that energy was blocked from propagating eastward by the deformation region. Time series of the deformation and downstream development terms from 11 to 15 February are negatively correlated ( $r = -.77$ ), another suggestion that the two terms were governed by the same characteristic of the environment: the deformation region and associated weak background QGPV gradient. While Terms *i* and *ii* oppose each other in general (Figure 2a vs. Figure 3), this inverse relationship between their influence on *growth* has not been found by previous studies employing PTD.

Mak and Cai (1989) discussed how the shape and orientation of eddies with respect to deformation influences the barotropic energy exchange between eddies and the background state kinetic energy. The right combination of eddy shape and deformation can allow eddies to extract energy from the kinetic energy of the environment. Evans and Black (2003) interpreted growth from the barotropic deformation

term in the PTD framework as evidence of barotropic growth, which they found was important for developing cyclones and anticyclones in the Atlantic region. The life cycle of Feature A, dominated by the deformation term and also responsible for a weakening of the kinetic energy of the mean state, provides additional evidence for a connection between barotropic growth and a weakened zonal jet.

Shutts (1983) demonstrated how deformation associated with a block led to a vorticity flux forcing on the zonal wind that maintained the block. His figure 1 shows how eddies approaching the deformation and block are stretched out and weakened within the block itself, as observed in this case on 14 February. It is suggested through PTD that this evolution can be captured through a change in sign of the deformation and downstream development terms, and the coincidence of deformation both weakening the ridge by stretching it out *and* preventing the downstream propagation of Rossby wave energy.

More recently, studies have investigated the role of diabatic heating associated with latent heat release, and how it impacts the development of anticyclones (Pfahl *et al.*, 2015; Teubler and Riemer, 2016). The vertical distribution of diabatic heating is associated with a direct effect on the PV field, and also an indirect effect through the production of upper-level divergence which can transport low PV across isentropic surfaces (Teubler and Riemer, 2016). One caveat to the inversion method employed here as introduced by NGL is that it assumes adiabatic motion. However, Evans and Black (2003) expanded the traditional PTD to quantify the direct diabatic effect on PV, as well as the influence of ageostrophic motion on height tendencies. They did not find a dominant influence from any of these terms over the life cycle of North Pacific anticyclones. It was found in this case, similar to the results of Evans and Black (2003) and Teubler and Riemer (2016), that the direct diabatic effect on Feature A's development was an order of magnitude smaller than the other terms (not shown). Investigation of the influence of the divergent wind on the QGPV field is beyond the scope of this study, but given the influence of the PV intrusion, and its geostrophic advection early in A's life cycle, the authors conclude that divergent outflow and its influence on the QGPV was not *necessary* for the initial development of Feature A. The discussion of the PV intrusion's role in A's preliminary development was indeed intended to highlight that the presence of divergent outflow is not the only way to induce the development of anticyclones equatorward of the jet.

Returning to consideration of the composite flow evolution during jet retractions (Figure 1), many previously elusive features can now be placed in an emerging dynamical context. An extended jet accompanied by a high-amplitude ridge in the exit region sets up an environment conducive to initiating a retraction by forming a region of strong deformation. The negative PV anomaly on the cyclonic shear side of the jet in the composite (Figure 1b), B in this case, encounters the jet

entrance region, at which point it initiates a positively-tilted, southeastward-directed wave train, leading to the growth of a ridge, Feature A, in the subtropics. A's subsequent development marks the beginning of the disruption of the zonal jet. Meanwhile, the subtropical waveguide (345 K, Figure 5) is displaced southward and is characterized by a strip of synoptic-scale, cyclonic PV anomalies to the south of the sprawling anticyclone, accounting for the zonally extended but meridionally confined cyclonic PV anomaly observed in the composite. This subtropical component represents the southern branch of the split flow observed during Rex blocking events, and in this case was related to a period of persistent rainfall over Hawaii. Preliminary diagnosis of other jet retractions indicates the role of deformation may be common among the jet retractions identified by Jaffe *et al.* (2011). A subsequent article will complement the information gained through application of traditional PTD with an expanded PTD method to analyse zonal wind tendencies in a piecewise manner. Ongoing and future work will employ an independent method, a linear inverse model, to investigate the predictability of retractions and the dipole-type block that follows retraction.

#### ACKNOWLEDGEMENTS

The authors would like to acknowledge the many suggestions of Prof. Michael Morgan regarding both the QGPV inversion methodology as well as interpretation of the results of this study. We would also like to thank the National Science Foundation for supporting this research through Grant AGS-1265182.

#### ORCID

Melissa Breeden  <http://orcid.org/0000-0001-6298-3696>

#### REFERENCES

- Athanasiadis, P.J., Wallace, J.M. and Wettstein, J.J. (2010) Patterns of wintertime jet stream variability and their relation to the storm tracks. *Journal of the Atmospheric Sciences*, 67, 1361–1381. <https://doi.org/10.1175/2009JAS3270.1>.
- Barnston, A.G. and Livezey, R.E. (1987) Classification, seasonality and persistence of low-frequency atmospheric circulation patterns. *Monthly Weather Review*, 115, 1083–1126.
- Berrisford, P., Dee, D.P., Poli, P., Brugge, R., Fielding, K., Fuentes, M., Källberg, P.W., Kobayashi, S., Uppala, S. and Simmons, A. (2011) *The ERA-Interim archive version 2.0*. ERA Report Series 1. Available at: <http://www.ecmwf.int/en/elibrary/8174-era-interim-archive-version-20> [Accessed 9 September 2017]
- Bretherton, F.P. (1966) Critical layer instability in baroclinic flows. *Quarterly Journal of the Royal Meteorological Society*, 92, 325–334.
- Charney, J.G. and Stern, M.E. (1962) On the stability of internal baroclinic jets in a rotating atmosphere. *Journal of the Atmospheric Sciences*, 19, 159–172.
- Climate Prediction Center Internet Team, National Centers for Environmental Prediction Climate Prediction Center. (2005) *Pacific/North American pattern*, December 12, 2005. Available at: <http://www.cpc.ncep.noaa.gov/products/precip/CWlink/pna/pna.shtml> [Accessed 8 November 2015]
- Dee, D.P., Uppala, S.M., Simmons, A.J., Berrisford, P., Poli, P., Kobayashi, S., Andrae, U., Balmaseda, M.A., Balsamo, G., Bauer, P., Bechtold, P., Beljaars, A.C.M., van de Berg, L., Bidlot, J., Bormann, N., Delsol, C., Dragani, R., Fuentes, M., Geer, A.J., Haimberger, L., Healy, S.B., Hersbach, H., Hólm, E.V., Isaksen, I., Kållberg, P., Köhler, M., Matricardi, M., McNally, A.P., Monge-Sanz, B.M., Morcrette, J.-J., Park, B.-K., Peubey, C., de Rosnay, P., Tavolato, C., Thépaut, J.-N. and Vitart, F. (2011) The ERA-Interim reanalysis: configuration and performance of the data assimilation system. *Quarterly Journal of the Royal Meteorological Society*, 137(656), 553–597. <https://doi.org/10.1002/qj.828>.
- Dole, R. and Gordon, N.D. (1983) Persistent anomalies of the extratropical Northern Hemisphere wintertime circulation: geographical distribution and regional persistence characteristics. *Monthly Weather Review*, 111, 1567–1586.
- Eichelberger, S.J. and Hartmann, D.L. (2007) Zonal jet structure and the leading mode of variability. *Journal of Climate*, 20, 5149–5163.
- Evans, K.J. and Black, R.X. (2003) Piecewise tendency diagnosis of weather regime transitions. *Journal of the Atmospheric Sciences*, 60, 1949–1959.
- Federal Emergency Management Agency. (2006) *Hawaii Severe Storms, Flooding, Landslides, and Mudslides (DR-1640)*, September 12, 2006. Available at: <https://www.fema.gov/disaster/1640#tabs-2> [Accessed 27 February 2017]
- Fleming, E.L., Lim, G.-H. and Wallace, J.M. (1987) Differences between the spring and autumn circulation of the Northern Hemisphere. *Journal of the Atmospheric Sciences*, 44, 1266–1286.
- Franzke, C., Feldstein, S.B. and Lee, S. (2011) Synoptic analysis of the Pacific–North American teleconnection pattern. *Quarterly Journal of the Royal Meteorological Society*, 137, 329–346.
- Griffin, K.S. and Martin, J.E. (2017) Synoptic features associated with temporally coherent modes of variability of the North Pacific jet stream. *Journal of Climate*, 30, 39–54.
- Hakim, G.J., Bosart, L.F. and Keyser, D. (1996) The Ohio Valley wave-merger cyclogenesis event of 25–26 January 1978. Part II: Diagnosis using quasi-geostrophic potential vorticity inversion. *Monthly Weather Review*, 124, 2176–2205.
- Holopainen, E. and Kaurola, J. (1991) Decomposing the atmospheric flow using potential vorticity framework. *Journal of the Atmospheric Sciences*, 48, 2614–2625.
- Jaffe, S.C., Martin, J.E., Vimont, D.J. and Lorenz, D.J. (2011) A synoptic-climatology of episodic, sub-seasonal retractions of the Pacific jet. *Journal of Climate*, 24, 2846–2860.
- Jayawardena, I.M., Chen, Y.L., Nash, A.J. and Kodama, K. (2012) A comparison of three prolonged periods of heavy rainfall over the Hawaiian Islands. *Journal of Applied Meteorology*, 51, 722–744.
- Mak, M. and Cai, M. (1989) Local barotropic instability. *Journal of the Atmospheric Sciences*, 46, 3289–3311.
- Martius, O., Schwierz, C. and Davies, H.C. (2007) Breaking waves at the tropopause in the wintertime Northern Hemisphere: climatological analyses of the orientation and the theoretical LC1/2 classification. *Journal of the Atmospheric Sciences*, 64, 2576–2592.
- McIntyre, M.E. and Palmer, T.N. (1983) Breaking planetary waves in the stratosphere. *Nature*, 305, 593–600.
- Morgan, M.C. and Nielsen-Gammon, J.W. (1998) Using tropopause maps to diagnose midlatitude weather systems. *Monthly Weather Review*, 126, 2555–2579.
- Namias, J. and Clapp, P.F. (1949) Confluence theory of the high tropospheric jet stream. *Journal of Meteorology*, 6, 330–336.
- Newman, M. and Sardeshmukh, P.D. (1998) The impact of the annual cycle on the North Pacific/North American response to remote low-frequency forcing. *Journal of the Atmospheric Sciences*, 55, 1336–1353.
- Nielsen-Gammon, J.W. and Lefèvre, R.J. (1996) Piecewise tendency diagnosis of dynamical processes governing the development of an upper-tropospheric mobile trough. *Journal of the Atmospheric Sciences*, 53, 3120–3142.
- Otkin, J.A. and Martin, J.E. (2004) The large-scale modulation of subtropical cyclogenesis in the central and eastern Pacific Ocean. *Monthly Weather Review*, 132, 1813–1828.
- Palmén, E. (1948) On the distribution of temperature and winds in the upper westerlies. *Journal of Meteorology*, 5, 20–27.
- Palmén, E.H. and Newton, C.W. (1969) *Atmospheric Circulation Systems*, Vol. 13. Cambridge, MA: Academic Press.
- Pelly, J.L. and Hoskins, B.J. (2003) A new perspective on blocking. *Journal of the Atmospheric Sciences*, 60, 734–755.

- Pfahl, S., Schwierz, C., Croci-Maspoli, M., Grams, C.M. and Wernli, H. (2015) Importance of latent heat release in ascending air streams for atmospheric blocking. *Nature Geoscience*, 8, 610–614.
- Rex, D.F. (1950) Blocking action in the middle troposphere and its effect upon regional climate. *Tellus*, 2–3, 196–211.
- Shutts, G.J. (1983) The propagation of eddies in diffluent jetstreams: eddy vorticity forcing of “blocking” flow fields. *Quarterly Journal of the Royal Meteorological Society*, 109, 737–761.
- Simmons, A.J. and Hoskins, B.J. (1980) Barotropic influences on the growth and decay of nonlinear baroclinic waves. *Journal of the Atmospheric Sciences*, 37, 1679–1684.
- Teubler, F. and Riemer, M. (2016) Dynamics of Rossby wave packets in a quantitative potential vorticity–potential temperature framework. *Journal of the Atmospheric Sciences*, 73, 1063–1081. <https://doi.org/10.1175/JAS-D-15-0162.1>.
- Thorncroft, C.D., Hoskins, B.J. and McIntyre, M.E. (1993) Two paradigms of baroclinic-wave life-cycle behaviour. *Quarterly Journal of the Royal Meteorological Society*, 119, 17–55.
- Wallace, J.M. and Gutzler, D.S. (1981) Teleconnections in the geopotential height field during the Northern Hemisphere winter. *Monthly Weather Review*, 109, 784–812.
- Weickmann, K.M. and Chervin, R.M. (1988) The observed and simulated atmospheric seasonal cycle. Part I: Global wind field modes. *Journal of Climate*, 1, 265–289.

**How to cite this article:** Breeden M, Martin JE. Analysis of the initiation of an extreme North Pacific jet retraction using piecewise tendency diagnosis. *Q J R Meteorol Soc.* 2018;144:1895–1913. <https://doi.org/10.1002/qj.3388>